Nanoscale

ROYAL SOCIETY OF CHEMISTRY

REVIEW

View Article Online
View Journal | View Issue

Cite this: *Nanoscale*, 2020, **12**, 23371

Printed carbon nanotube thin-film transistors: progress on printable materials and the path to applications

Shiheng Lu [a] and Aaron D. Franklin *[a,b]

Printing technologies have attracted significant attention owing to their potential use in the low-cost manufacturing of custom or large-area flexible electronics. Among the many printable electronic materials that have been explored, semiconducting carbon nanotubes (CNTs) have shown increasing promise based on their exceptional electrical and mechanical properties, relative stability in air, and compatibility with several printing techniques to form semiconducting thin films. These attractive attributes make printed CNT thin films promising for applications including, but not limited to, sensors and display backplanes – at the heart of which is electronics' most versatile device: the transistor. In this review, we present a summary of recent advancements in the field of printed carbon nanotube thin-film transistors (CNT-TFTs). In addition to an introduction of different printing techniques, together with their strengths and limitations, we discuss key aspects of ink/material selection and processing of various device components, including the CNT channels, contacts, and gate insulators. It is clear that printed CNT-TFTs are rapidly advancing, but there remain challenges, which are discussed along with current techniques to resolve them and future developments towards practical applications from these devices. There has been interest in low-cost, printable transistors for many years and the CNT-TFTs show great promise for delivering, but will not become a reality without further research advancement.

Received 28th August 2020,
Accepted 15th November 2020

DOI: 10.1039/d0nr06231f

rsc.li/nanoscale

[a]*Department of Electrical and Computer Engineering, Duke University, Durham, NC 27708, USA. E-mail: aaron.franklin@duke.edu*
[b]*Department of Chemistry, Duke University, Durham, NC 27708, USA*

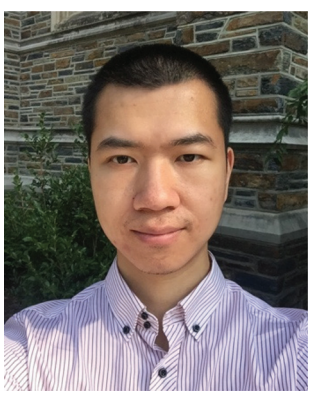

Shiheng Lu

Shiheng Lu received the B.S. degree in Physics from Fudan University in 2016 and the M.S. degree in Electrical Engineering from Stanford University in 2018. He is currently pursuing the Ph.D. degree in electrical engineering with Duke University. His research focuses on printed electronics with an emphasis on developing low-temperature, stable printing processes using nanomaterial-based inks.

Aaron D. Franklin

Aaron Franklin is the Addy Professor of Electrical & Computer Engineering and Chemistry at Duke University. He received his Ph.D. in Electrical Engineering from Purdue University in 2008 and then spent six years on the research staff at the IBM T. J. Watson Research Center working on carbon nanomaterial-based transistors. In 2014, he joined the faculty at Duke where his group has three primary research thrusts: (1) nanomaterials in high-performance nanoelectronic devices, (2) nanomaterial inks for low-cost printed electronics, and (3) harnessing nanomaterial sensitivity in biomedical sensing systems. He has been actively involved in technology translation into start-up companies and holds more than 50 issued patents.

1. Introduction

The expansive development of the Internet-of-Things (IoT), combined with the growing benefits of machine learning from large datasets, is generating countless new improvements and solutions to major societal and environmental challenges. As society grows ever more capable of using large sets of data, the appetite for low-cost, readily customizable electronics to collect and process data grows. With the IoT now giving way to the Internet-of-Everything (IoE), the drive has increased for flexible radio frequency identification (RFID) tags, sensors, displays, memories, and other versatile electronics devices.[1] Traditional CMOS technology has demonstrated its exceptional ability in producing high-performance integrated circuits on aggressively miniaturized chips for computation and memory storage. However, for CMOS technology, large areas and/or small volumes of custom devices usually result in high cost and/or low throughput. Thus, traditional cleanroom fabrication techniques may not be the best choice for large-area flexible electronic components, where there is no need to pack nanoscale transistors on a centimeter-scale chip with high density and accuracy. In addition, a number of high-temperature processing steps and harsh chemical treatments are included in cleanroom technology, posing limitation to the substrate compatibility. Printing technologies, despite their limited resolution, offer substantially lower cost and higher throughput along with the ability to enable ready customization in device/circuit design. In addition, printing is compatible with a great variety of flexible substrates, including plastic,[2] paper,[3] and textiles,[4] thus making it an excellent candidate for large-area or custom flexible electronics—the gaps left by traditional CMOS technology.

The use of printing technologies for large-area or custom electronics has motivated researchers based on its potential in low-cost and high-throughput manufacturing. A great variety of printing methods have been explored, including template-based gravure and screen printing,[2,5] as well as direct-write methods such as inkjet and aerosol jet printing.[6] Being the base unit of digital circuits and playing a crucial role in sensing,[6] displays,[5] and RF applications,[2] transistors have received the greatest level of research attention when exploring the potential of printed electronic thin films. What's more, a transistor requires the appropriate combination of conducting, semiconducting, and insulating materials in order to achieve proper function and respectable performance. Representative semiconducting materials for printed thin-film transistors (TFTs) include organic semiconductors,[7–11] metal oxides,[11–14] and semiconducting single-walled carbon nanotubes (CNTs).[15–19]

A summary of printed semiconducting thin films is shown in Fig. 1a and b. The organic semiconductors for printed TFTs possess much lower mobility compared to CNTs and metal oxides, leading to low drive current, which is a hindrance for most applications;[7–11] not to mention the fact that most organic semiconductors suffer from poor air stability.[20] TFTs with printed metal oxides offer mobility and gate tunability comparable to those with CNTs, but most of the printed metals oxides rely on high-temperature (300–500 °C) annealing to become functional, precluding their use on many low-cost yet temperature-sensitive flexible substrates such as polyethylene terephthalate (PET).[11–14] Low-temperature deposition of metal–oxide semiconducting thin films has been achieved *via* cleanroom techniques such as atomic layer deposition (ALD);[21] however, the high cost and low throughput of such vacuum deposition methods limit the potential application for large-area electronics.

In addition, recent developments in the solution-phase preparation of 2D material inks have facilitated demonstrations of printed TFTs based on 2D materials, such as graphene and transition metal dichalcogenides (TMDs).[22–26] Printed graphene exhibits respectable mobility up to 95 cm^2 V s^{-1}, but its zero-bandgap nature leads to poor on/off-current ratios (<10), thus hampering the use in digital circuits.[22,23] Printed TMDs, on the other hand, offer reasonable current modulation, but their mobility at the present stage ranges from 0.01–0.1 cm^2 V s^{-1}, around 2 orders of magnitude lower than CNTs and metal oxides.[24–26]

Printed CNTs, in comparison, offer among the highest on-state current and gate tunability with no harsh thermal treatment required (Fig. 1a and b). Hence, TFTs with printed CNT thin-film channels are very attractive for cost-effective printing of large-area or customizable electronics. Examples of demonstrations from printed CNT-TFTs include active-matrix backplanes for large-area displays (Fig. 1c)[17] and addressable multi-touch sensors,[27] as well as flexible circuits for digital logic[28] and radio frequency identification (RFID) tags (Fig. 1d).[2] In addition, the nanostructured CNTs exhibit large surface-to-volume ratio, which is a useful attribute for sensing applications (Fig. 1e).[6] The networked structure of CNT channels also enables stretchability, making CNT-TFTs viable for stretchable applications like wearable electronics and electronic skin.[29]

In this review article, we summarize the progress made towards printed CNT-TFT technologies, highlighting advancements in material selection and processing for different device components, and discuss challenges that require further attention to bring these technologies closer to a commercial reality. The remainder of the article consists of 5 sections. In section 2, we provide a summary of different printing methods, discussing their working principles and feasible scopes of application. Section 3 outlines the purification, pre-deposition, and post-deposition processing techniques developed for CNTs and their printed thin films. Different printable materials for contact electrodes, as well as recent advancements in contact engineering and benchmarking, are summarized in section 4. In section 5, we discuss the printable gate insulator for CNT-TFTs, together with the applications facilitated by the unique properties of these insulators. Finally, in section 6, we present an outlook for CNT-TFT printing, including an outline of current challenges related to printing stability, device variability, and benchmarking, as well as a discussion of opportunities moving forward.

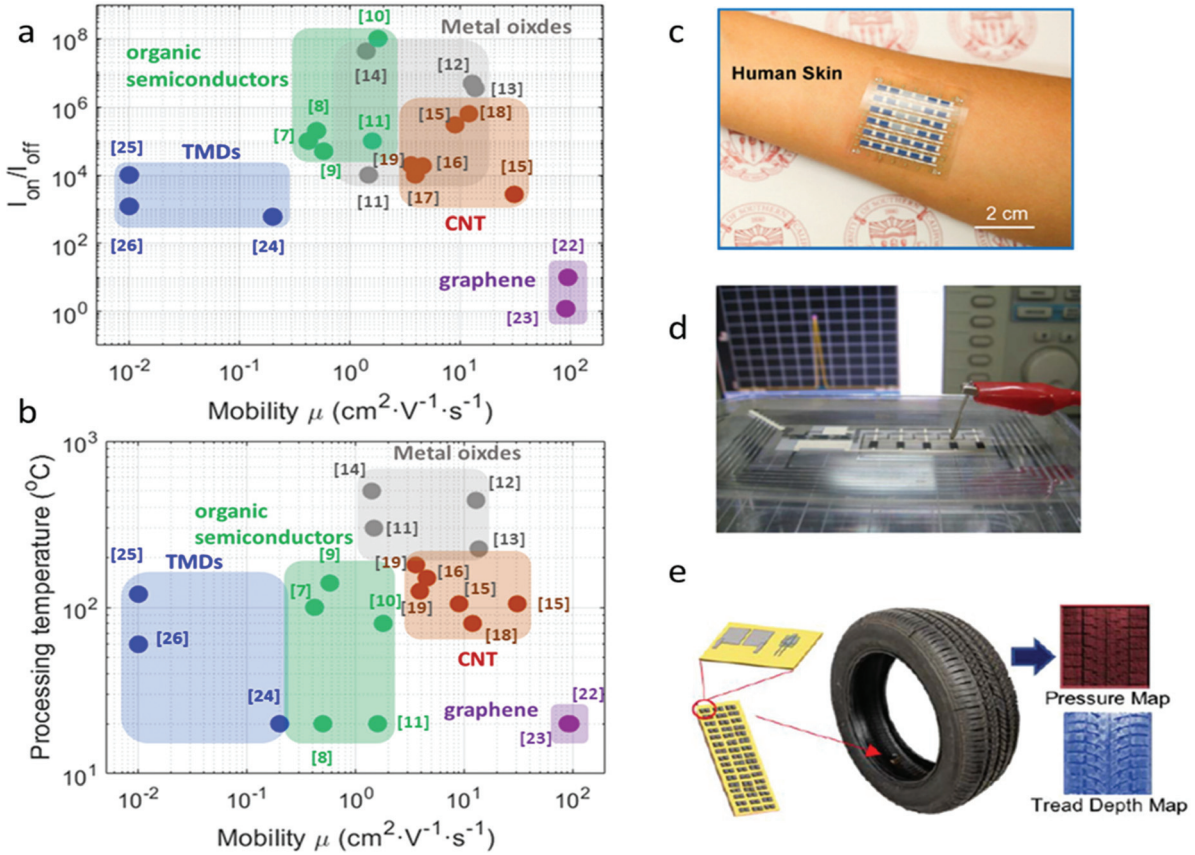

Fig. 1 (a) and (b) Comparison between the mobility, on/off-current ratio, and maximum processing temperature of different printed semiconducting thin films. (c) Photo of an electrochromic display with a CNT-TFT active-matrix backplane. (d) Photo of a printed RFID tag. (e) Schematic diagram and photo illustrating a CNT-TFT-based tire pressure sensor. (c) Adapted with permission from ref. 17. Copyright (2016) American Chemical Society. (d) Adapted with permission from ref. 2. Copyright (2010) IEEE. (e) Adapted with permission from ref. 6. Copyright (2018) IEEE.

2. Printing strategies

The early printed carbon nanotube transistors were almost always partially printed; *i.e.*, some device layers are deposited and/or patterned *via* non-printing techniques, such as thermal evaporation and photolithography.[15] In addition, there usually exist some processing steps that require removing the substrate from the printing system for external processing throughout the entire fabrication process flow, even for a so-called 'fully printed CNT-TFT'. Examples of these processing steps include washing or annealing for carbon nanotubes, sintering for contact materials, and curing for gate dielectrics. These steps have drastically limited the low-cost, high-throughput nature of printing technologies, and developments in printable materials have been made in recent years to get rid of these steps and realize true 'in-place printing',[18,30] which will be further discussed in section 5. As for the printing techniques that have been used for establishing CNT-TFTs, they generally fall into two categories: template-based roll-to-roll (R2R) printing and direct-write printing.

2.1. Template-based roll-to-roll printing

Like traditional newspaper printing, template-based printing requires a template to define the ink pattern printed onto the substrates. Prevalent template-based printing methods include gravure printing, screen printing, and slot-die printing. While there are reports of slot-die-printed metallic nanotube electrodes[31] and screen-printed CNT-TFTs,[5,17] gravure printing is among the most prevalent template-based printing methods for CNT-TFTs to date.[27,28,32–36] As shown in Fig. 2a, gravure printing includes a cylindrical carrier with engraved patterns as the template. As the cylinder keeps rolling, the inks are picked up by the carrier, and a blade is involved to remove the excess inks, only leaving those in the engraved patterns. Pressure is applied between the cylinder and the substrate to help transfer the inks from the carrier to the substrate.[37] One of the most promising aspects of template-based printing is its extremely high throughput facilitated by its roll-to-roll compatibility. While the R2R printing speed of CNT-TFTs is usually hindered by the CNT deposition step due to difficulties with viscosity modification of CNT inks, there have been reports on full R2R printing of organic polymer transistors with printing speed at the order of 1 m s^{-1} and sub-10 μm resolution.[7]

Indeed, one of the foremost challenges of R2R gravure printing for CNT-TFT fabrication is that it requires the ink viscosity to be much higher than the solvents commonly used to disperse CNTs, such as toluene, chloroform, *o*-xylene, or di-

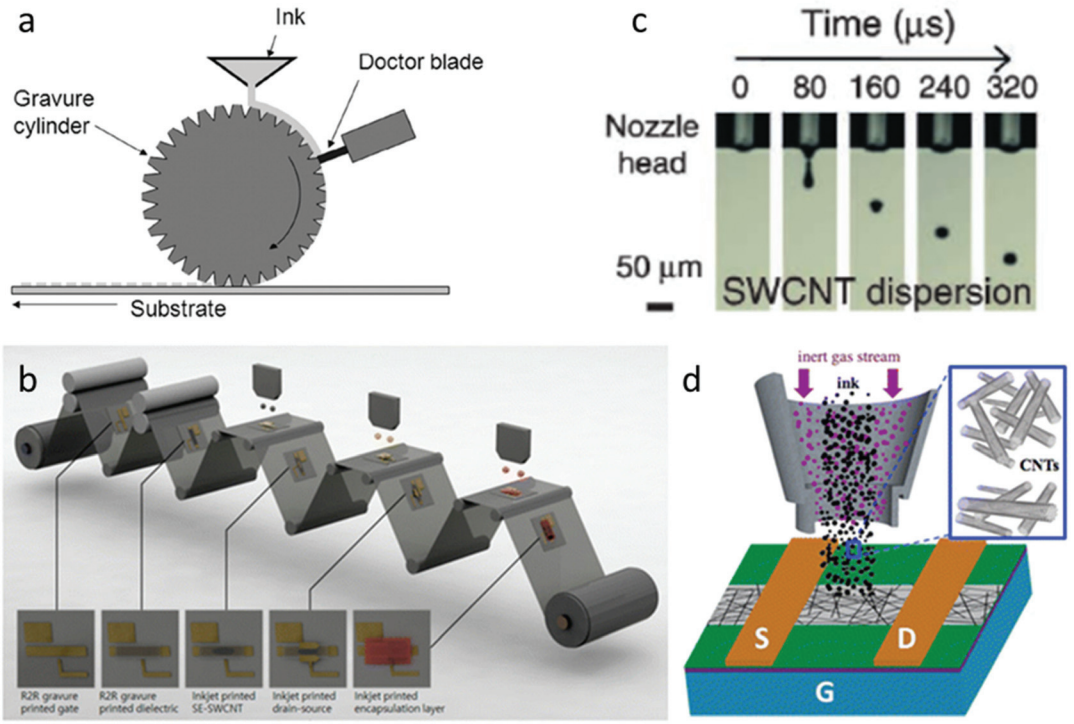

Fig. 2 Printing methods for CNT-TFT fabrication. (a) Schematic diagram illustrating the working principle of gravure printing. (b) Schematic diagram illustrating gravure- and inkjet-based R2R printing of a CNT-TFT. (c) Time-dependent snapshots of an inkjet-printed CNT ink droplet. (d) Schematic diagram illustrating aerosol jet printing of a CNT-TFT. (a) Adapted with permission from ref. 37. Copyright (2010) IEEE. (b) Adapted with permission from ref. 33. Copyright (2016) American Chemical Society. (c) Adapted with permission from ref. 38. Copyright (2010) Wiley. (d) Adapted with permission from ref. 122. Copyright (2016) American Chemical Society.

methylformamide (DMF). One solution is to add binders to the CNT inks to make them more viscous and printable using R2R gravure. However, the presence of binders, which are polymers in most cases, could drastically lower the performance of printed CNT films. Another solution is to integrate other CNT deposition methods, such as inkjet printing,[32–34] roll-to-plate gravure printing,[35,36] or spray coating,[28] into the gravure-based R2R printing system. For instance, as shown in Fig. 2b, the CNT film, source (S) and drain (D) electrodes, and the encapsulation layer are inkjet-printed, while the remaining layers of the device are deposited *via* gravure printing.[33] The whole process flow is still R2R without adding any binders that could potentially degrade the resultant device performance, but the overall printing speed is now gated by the inkjet printing steps.

While the viscosity issue seems to be specific for CNTs (and other materials whose ink viscosity is low), there is another more universal and fundamental limitation of template-based printing: the template needs to be manufactured for every individual design. While the cost of the template can be averaged out by mass production, in the case of prototyping or other settings where the device and circuit layout needs to be modified readily, the cost of the frequently updated templates is a bottleneck.

2.2. Direct-write printing

In comparison to template-based printing, direct-write printing does not require any template to determine the pattern. Instead, the inks are extruded or ejected from a print nozzle onto the substrate on-demand, and by moving the substrate or the nozzle, inks are deposited onto the targeted locations and form desired patterns. The movement of the nozzle or the substrate is controlled by certain files depending on the manufacturer of the printer. These files can be easily modified with negligible cost. Although not as high-throughput as template-based printing, the direct-write methods possess high design flexibility, with higher throughput compared to cleanroom fabrication techniques, thus filling the blank of prototyping and research left by template-based printing.

2.2.1. Inkjet printing. Inkjet printing is the most prevalent direct-write method for printed electronics. As shown in Fig. 2c, by applying a mechanical pulse (*e.g.*, *via* a piezoelectric transducer) the inks are pushed out from the nozzle and form a droplet directed to the substrate.[38] By controlling the nozzle movement and pulse frequency, droplets are formed and jetted to the wanted position with tunable spacing—drop-on-demand. The formation of ink droplets and their ejection from the nozzle depends on both the nozzle size and the ink's physical properties, including density, viscosity, and surface tension. The dimensionless inverse Ohnesorge number Z is commonly adopted to analyze the droplet formation and thus to evaluate the inkjet-printability of certain inks.[39] For inkjet printing, $Z = \sqrt{\gamma\alpha\rho}/\eta$, where α is the nozzle diameter, and γ, ρ and η refer to the ink's surface tension, density, and viscosity,

respectively. While technological advancements have been made such that stable droplet formation with low viscosity ink and Z larger than 20 has been achieved,[40] Z values satisfying $4 \leq Z \leq 14$ are usually expected to offer stable droplet formation. Z values smaller than 4 gives slow droplet formation with long tails, whereas satellite droplets occur at $Z > 14$.[41]

For inkjet-printed inks whose viscosity is usually lower than 30 cP, the so-called coffee ring effect typically appears, where most of the solutes are distributed near the edge of the initial droplet and form a ring pattern after drying.[19,42] A widely accepted explanation of this phenomenon is that the solvent evaporates faster at the edge of the droplet during the drying process, thus causing an outward flow from the droplet center that replenish the evaporated solvent. The flow carries the solute to the perimeters and forms the coffee rings.[43] This phenomenon is usually undesirable as it deteriorates the uniformity of the printed films and might worsen the resultant device performance. The alleviation of this unwanted effect could be achieved by either ink formulation or substrate modification. For instance, adding a secondary solvent, such as 2-butanol in isopropyl–alcohol-based ink, could introduce a Marangoni flow, counterbalancing the outward flow that produces the coffee ring effect.[42,44] There has also been an observation that aminopropyltriethoxy silane (APTES)-treatment on SiO_2 substrate suppresses the coffee ring effect and produces homogenous deposition of an aqueous CNT ink.[19]

During the inkjet printing process, the ink is in direct contact with the nozzle sidewall, raising the propensity of nozzle clogging. In particular, for nanomaterial-based inks, the average particle size should be smaller than 1/50 of the nozzle diameter to ensure stable printing.[45] For instance, the particle size should be no more than 400 nm for a typical 21 μm nozzle. This limit is especially unfavorable for the cases where size-dependent effects, such as percolation transport of nanotube or nanowire networks, play a role.[46]

2.2.2. Aerosol jet printing. Aerosol jet printing is another direct-write method with its working mechanism illustrated in Fig. 2d. The ink loaded in the atomizer is "atomized" (*i.e.*, aerosolized), either pneumatically or ultrasonically, into an aerosol mist and is carried towards the deposition head by a carrier gas flow. In the deposition head, the stream is focused by a sheath gas flow and jetted onto the substrate to form the wanted pattern. The sheath flow prevents direct contact between the ink and the nozzle sidewall, thus reducing the risk of nozzle clogging and enhancing printing stability.[47] This makes aerosol jet printing especially suitable for printing nanomaterials. In addition, compared to inkjet printing, aerosol jet printing is compatible with a broad range of ink viscosity from 1 to 1000 cP, enabling rigorous ink formulation.[48]

The focusing ratio (*i.e.*, the sheath flow rate over carrier gas flow rate) plays a crucial role in the resulting trace morphology,[49] and the amount of ink deposited is tuned by modifying the printing speed, the carrier gas flow rate, and the number of passes. Like inkjet printing, coffee ring effects may also occur in aerosol jet printing. While not desirable in most cases, there have been a few studies that intentionally utilize this effect to realize certain structural or electrical properties. For instance, preferentially aligned CNT twin-lines driven by the same outward flow from the middle of the printed trace has been obtained using aerosol jet printing.[50]

Another advantage to the aerosol jet printing technique is that the volume of solvent that must be dried from the aerosolized droplets is much lower than in a single inkjet droplet, allowing for more rapid dry times and customizable diffusion rates based on control of the thermal environment of the printer. However, unlike individual droplets jetted in inkjet printing, the ejection of continuous, focused aerosol mist includes the downside of overspray, which can result in spots or traces that are not as well-defined compared to inkjet printing.[51] Although such phenomenon could be minimized by ink formulation and proper tuning of the printing parameters, overspray cannot be fully eliminated, and all of its underlying mechanisms are still not fully understood.[49]

3. Carbon nanotube processing: from inks to thin films

Although not related to its synthesis in reality, a single-walled carbon nanotube (CNT or SWCNT) can be thought of as a monolayer graphene sheet rolled up along a certain direction (or lattice/chiral vector) to form a cylindrical tube. Similarly, multi-walled carbon nanotube (MWCNT) can be considered as many coaxial SWCNTs with different diameters or a single graphene sheet rolled up around an axis for multiple cycles. An individual SWCNT can exhibit near-ballistic transport[52] with field-effect mobility as high as 79 000 $cm^2\ V\ s^{-1}$ reported.[53] Carrier transport in the networked SWCNT thin films, on the other hand, follows percolation transport and is dominated by the resistive tube–tube junctions.[54,55] As a result, the network density of a CNT film needs to exceed a percolation threshold to ensure the existence of conducting pathways between electrical contacts, and the current flow through the network as well as the effective field-effect mobility are directly affected by the tube density. The effective field-effect mobility of a CNT thin film, usually ranging from 1 to 100 $cm^2\ V\ s^{-1}$, is much lower compared to the individual tubes due to the junctions. Nonetheless, it still exceeds most of the semiconducting materials for thin-film applications (see Fig. 1a and b), as discussed previously in the introduction section.

The electrical properties of a CNT are determined by its chirality featured by the lattice or chiral vector (m, n) along which the nanotube is 'rolled up': when $m - n \neq 3x$ (x is an integer), the tube is semiconducting, otherwise it's metallic and cannot be turned off by applying a gate voltage.[56] What's more, the energy band gap of a semiconducting tube is also determined by its chirality and is inversely proportional to its diameter. For transistors based on CNT thin films, the existence of metallic paths can be catastrophic to the off-state performance, while a reasonable range of tube diameters tends to be quite tolerable.[57,58] Therefore, the priorities are to reduce

the metallic content within the network and control the film density to eliminate metallic pathways.

The synthesis of MWCNTs and SWCNTs were first reported in 1991 and 1993, respectively,[59,60] both realized by S. Iijima *et al. via* arc-discharge. Since then, a number of techniques to grow CNTs have been developed and examined, and the common CNT growing methods include arc-discharge, laser ablation, and chemical vapor deposition (CVD).[61] However, most of these methods result in a wide chirality distribution, which statistically means that ~1/3 of the grown tubes are metallic—a ratio that is not sufficient for semiconductor device fabrication. There have been novel advancements in chirality-controlled synthesis which yield a higher selectivity of semiconducting tubes, but these tend to have lower overall yield or throughput.[62,63] In addition, self-sorted CNT thin films can be obtained *via* selective adhesion of CNTs on substrates with certain functionalization.[64] However, the scalability or reproducibility offered by these as-grown or as-coated methods are currently still not sufficient for scaled-up manufacturing. Solution-based, post-growth separation of semiconducting CNTs, on the other hand, is potentially both scalable and high throughput.

3.1. Solution-based chirality sorting of CNTs

To separate the semiconducting CNTs or extract the tubes with certain chirality, researchers have explored separation methods ranging from gel chromatography[65–67] to density gradient ultracentrifugation (DGU)[68,69] and aqueous two-phase separation.[70] In addition, various chemicals that selectively bind to or wrap around the CNTs with certain chiralities have been proposed, synthesized, and examined to further enhance the selection. Examples include DNA,[65,66,71] flavin mononucleotide (FMN),[72] porphyrins,[73] and conjugated polymers such as derivatives of polyfluorene,[74–78] polythiophene,[78,79] and polycarbazole.[80] Among the great variety of sorting methods, selective dispersion with conjugated polymers has received specific attention due to its high selectivity, scalability, and yield (Fig. 3a–c).[74–80] Advancements have been made in the separation of CNTs with narrow chirality distribution or even monochirality. In particular, polyfluorene-based co-polymer poly [(9,9-dioctylfluorenyl-2,7-diyl)-*alt-co*-(6,6-(2,bipyridine))] (PFO-BPy) brings 96–97% enrichment of (6, 5) chirality with negligible metallic tubes remaining.[76] Side chain engineering has also been proposed to offer separation of semiconducting nanotubes with different diameters, as shown in Fig. 3a–c.[77,81]

In addition to the polymer, the sorting selectivity and the yield also strongly depend on the solvent. Studies have shown that non-polar solvents, such as toluene, *m*-xylene, *o*-xylene, and decalin, offer high selectivity due to their weak interaction with polarized metallic tubes, whereas solvents with large CNT dispersibility give high yield.[82] Toluene has been most frequently used due to its compatibility with a great variety of polymers.[74–79,81,83] *o*-Xylene, on the other hand, has been proposed as a strong alternative due to the significantly longer shelf-life presented by *o*-xylene-based CNT inks, comparable sorting results, and better wetting on SiO_2 substrates, which,

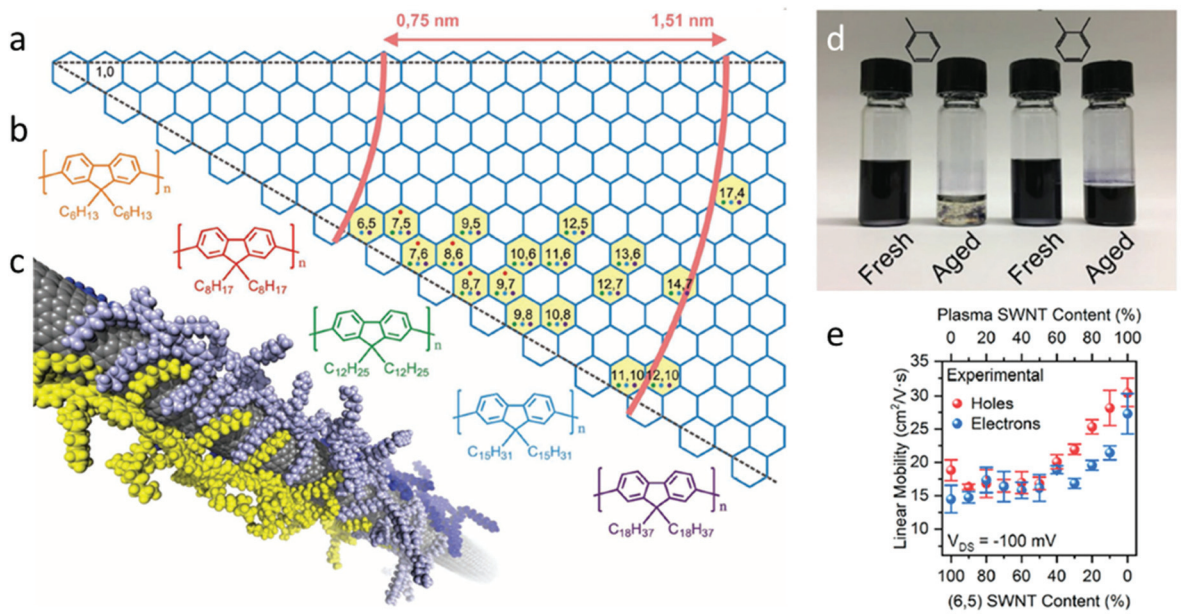

Fig. 3 Advancements in CNT sorting. (a) Chirality map of CNTs selected by various polyfluorene derivatives. (b) Chemical structures of the polyfluorene derivatives with various side chain lengths, from PF6 to PF18. (c) Molecular dynamics simulations of 3 PF8 molecules wrapping around a (12, 10) nanotube. (d) A photo of toluene- and *o*-xylene-based CNT inks before and after 1-year aging. (e) Electron and hole mobilities of CNT ("SWCNT") networks with various plasma SWCNT and (6, 5) SWCNT compositions. (a)–(c) Adapted with permission from ref. 77. Copyright (2013) Wiley. (d) Adapted with permission from ref. 84. Copyright (2019) Wiley. (e) Adapted with permission from ref. 88. Copyright (2019) American Chemical Society.

in turn, benefits the film homogeneity and the resultant device reproducibility on SiO_2, as illustrated in Fig. 3d.[84] In addition, a recent study achieved reasonable semiconducting purity (>99%) in a polar solvent (a mixture of methyl carbitol and toluene) by adopting polymer wrappers with hydrophobic backbone and hydrophilic side chains.[85] The advancement not only dramatically improves yield (up to 95%) without significantly sacrificing selectivity, but also offers more choices of solvent for further solution processing.

As mentioned earlier in this section, the presence of metallic tubes in a semiconducting network, together with its detrimental effects on resultant device performance, has been intensely investigated for over a decade,[57,58] and technological advancements have been made in sorting CNTs with narrow chirality distributions or even single chirality.[76,86] Driven by these advancements, the role of chirality and diameter distribution of the semiconducting tubes has received increasing attention during the past 5 years.[83,87,88] In particular, M. Rother *et al.* have found out that in a dense network consisting of CNTs with 2 different chiralities, the small-bandgap ones could dominate the carrier transport even if they are the minority.[87] This indicates that a small portion of large-diameter tubes in the dispersion or network could severely limit the performance (*e.g.*, mobility and on-current) of the resulting TFTs. In addition to the superiority of monochiral CNT networks, they also suggested that small-diameter tubes are preferential as impurities, when the presence of such is inevitable. Later, in a recent study, the same group reported that a thin film consisting of large-diameter (1.17–1.55 nm) tubes, despite the distribution of diameters and bandgaps, gives 2× higher effective mobility compared to the monochiral (6, 5) tubes, as illustrated in Fig. 3e.[88] Considering the relationship between on/off-current ratio and bandgap, they claimed that monochiral CNTs with reasonably large diameters (~1.2 nm) would be most ideal for TFT applications. These insights suggest important directions for future development of CNT sorting.

3.2. Processing of CNT dispersions/inks and films

For device fabrication, the solution-phase sorted CNTs are often deposited into networked or aligned films onto various substrates *via* drop-casting, spin-coating, or dip-coating; but the focus herein is on the use of printing. As discussed earlier in this section, a homogeneous film with proper density is desirable for device applications. Therefore, regardless of the deposition method, the adhesion between the tubes (with corresponding surfactants or wrappers) and the substrate plays a crucial role in CNT deposition. Studies have shown that amine-modified substrates provide strengthened adhesion to semiconducting tubes.[64] Therefore, substrate treatments using APTES or poly-L-lysine (PLL) solutions prior to CNT deposition are widely adopted to form self-assembled monolayers (SAM) that offer amine-functionalization to the substrate.[19,89,90] Interestingly, the presence of certain surfactants may block or limit the absorption of CNTs onto an amine-modified surface. For instance, excess alkyl-based surfactant within the CNT dispersion may bind to the amine sites, thus preventing further adhesion of surfactant-wrapped CNTs.[89] Some studies also show that anionic surfactants impede the CNTs from adhering to amine-functionalized surfaces, leading to sparse, discontinuous films and poor yield.[91] These observations provide restrictions and guidelines for the selection of substrate, solvent, and surfactant when developing CNT inks.

For CNTs sorted with polymer wrappers, it is inevitable to have polymer residue within the coated or printed CNT films, which can be problematic in many ways. For transistor applications, the residue may hinder carrier transport across tube–tube or tube-contact junctions, leading to low on-state current.[92,93] For sensing applications, moreover, the polymer wrappers may change the surface chemistry of the tube, which causes unwanted propagated impacts on the sensing performance.[94,95] Therefore, polymer removal is essential to maximize device performance.

One strategy is to reduce the polymer content within the CNT dispersion to its minimum before deposition; for instance, by centrifugation,[96] washing and filtering,[79,80,97] depolymerization[98–100] and conformation of the wrapper,[101] *etc*. It's worth noting that the complete removal of polymer wrappers might lead to CNT aggregation and precipitation (in solution),[99] and that some removal processes can be complex and time-consuming.[97] Nonetheless, with the proper selection of the wrapper and the processing technique, it is possible to achieve simple yet effective removal. For instance, it has been recently demonstrated that the content of the wrapper poly[9-(1-octylonoyl)-9*H*-carbazole-2,7-diyl] (PCz) can be effectively removed and recycled *via* a simple method based on (tetrahydrofuran) THF washing and filtering (Fig. 4a).[80] While a minimum amount of wrapper was still left in the dispersion, this method not only allows for the deposition of CNT films without further post treatment for many applications, but also promotes the recycling of polymer, reducing the overall cost and complexity of the entire process flow.

Another strategy is to remove the polymer content within the CNT film after printing or coating. While many novel and comparatively complex post treatments, such as metal–chelation-assisted polymer removal (McAPR)[100] and yttrium oxide coating/decoating,[102] have been recently demonstrated and proven effective for polymer removal, washing and annealing are still most widely used due to their simplicity, scalability, and low cost.[18,93,103–105]

Washing is carried out by rinsing or soaking the deposited networks with solvents that present high solubility[18,103,104] or are reactive with the selected polymer.[93] In particular, toluene has been most frequently used, and an elevated solvent temperature has been proven to offer more effective removal due to higher solubility and/or reactivity.[18,103] Annealing, on the other hand, provides strong removal while raising several concerns. A recent study has experimentally demonstrated that 400 °C annealing under high vacuum for an hour alone is as effective in the removal of polyfluorene wrappers as the same annealing process preceded by an additional toluene rinsing step.[104] Inevitably, the high processing temperature limits the

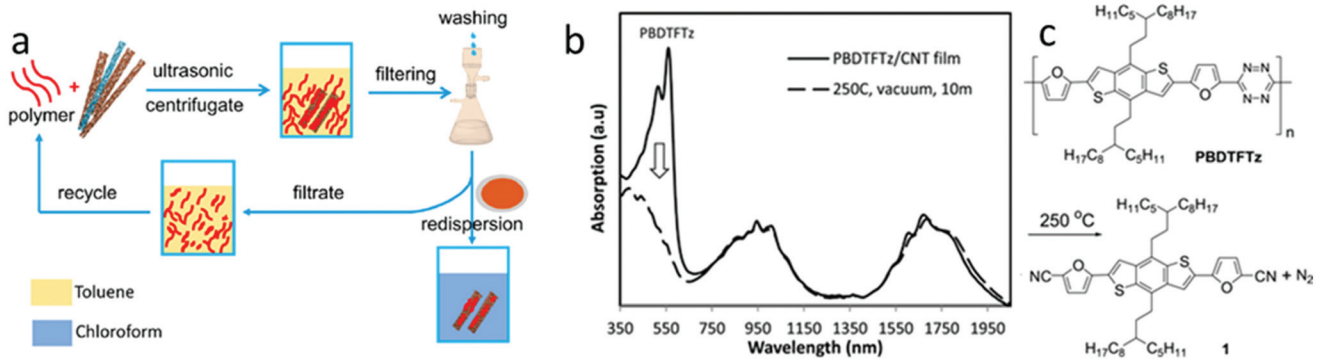

Fig. 4 Advancements in polymer removal from solution-processed CNTs. (a) Schematic illustrations of the washing-and-filtering methods to lower the polymer (PCz) content in CNT dispersion and to recycle PCz. (b) UV absorption spectra of a PBDTFTz-wrapped CNT film before and after 10 min annealing at 250 °C. (c) Decomposition reaction of PBDTFTz. (a) Adapted with permission from ref. 80. Copyright (2017) American Chemical Society. (b) and (c) Adapted with permission from ref. 95. Copyright (2018) Wiley.

use of annealing on most of the flexible substrates and increases the risk of additional detrimental defects in CNTs.[102] Nonetheless, recent studies have demonstrated that annealing is still one of the most effective polymer removal technique for printed CNTs, especially on thermally stable substrates, such as glass.[105] By replacing the wrapper with its easily decomposed alternatives *via* polymer exchange,[95] it is possible to lower the temperature requirement and make it compatible with a greater variety of substrates, as illustrated in Fig. 4b and c. Despite the added process complexity of the polymer exchange step, this advancement suggests that developing a sorting polymer with low decomposition temperature would be an interesting topic for future research. In addition, it's worth noting that washing and annealing can be combined to produce a stronger net effect,[104] and that it is common to adopt 2 strategies together: to remove the polymer component both before and after CNT deposition.[97,99]

3.3. Doping CNT thin films

Exposure to ambient air usually presents a p-type doping effect on the CNT transistors *via* oxygen and water adsorption,[106] and it is therefore much less challenging to obtain unipolar p-type CNT-TFTs compared to n-type. This hinders the use of CNT-TFTs in complementary circuits, which consist of transistors with both polarities and are advantageous in noise margin and power consumption.[107] Potassium metal has been used as an early n-type dopant for CNT transistors and diodes,[108] and for nanoelectronics or high-performance thin-film electronics based on cleanroom techniques, n-type CNT transistors can be realized *via* low-work function contact metals[109] or positively charged encapsulation layers like aluminium oxide[110] and silicon nitride.[111] A considerable number of solution-processable and printable dopants have also been experimentally demonstrated, including polyethyleneimine (PEI)[112] and several electron-donating small molecules.[107,113–118] In particular, groups led by Z. Bao and Y. Cui have demonstrated several inkjet-printable dopants based on benzoimidazole derivatives, and continuous and reliable threshold voltage tuning was obtained by controlling the doping concentrations (Fig. 5a and b).[117] It is shown in Fig. 5c and e that the complementary inverters enabled by the n-type doping present respectable performance, including large gains (up to 85) and noise margins (70% of $1/2V_{DD}$, where V_{DD} is the supply voltage). However, the reported n-type CNT-TFTs were not air-stable, despite the ability to recover device performance in a nitrogen atmosphere. Fortunately, many advancements were made on improving the environmental stability of CNT-TFTs treated with n-type dopants.[107,119,120] A recent study using aerosol jet printing to

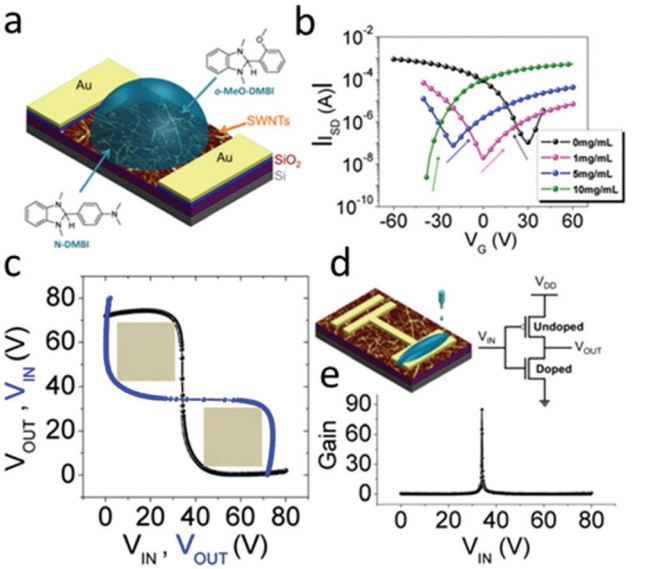

Fig. 5 Inkjet-based n-type doping for CNT-TFTs. (a) Schematic illustrations of a CNT-TFT doped with *o*-MeO-DMBI or N-DMBI. (b) Subthreshold characteristics of CNT-TFTs doped with various concentrations of *o*-MeO-DMBI. (c) Voltage transfer characteristics, (d) schematic illustration, and (e) gain of a *o*-MeO-DMBI doped complementary inverter. Adapted with permission from ref. 117. Copyright (2014) United States National Academy of Sciences.

deposit and pattern epoxy amine as the n-type dopants has achieved n-type CNT-TFTs with remarkable air stability, with only 30% change in on-current after 6 months of exposure in ambient conditions.[120] Aerosol-jet-printable ethanolamine inks, moreover, were reported to offer n-type doping to CNT-TFTs with decent air stability and enhanced performance in mobility, subthreshold swing and hysteresis compared to the original p-type CNT-TFTs.[107] In addition to the dopants directly coated or printed atop the CNT channel, recent studies also proposed another strategy where the dopants are directly added to the CNT dispersion before deposition.[121] This eliminates the extra fabrication step for doping, thus simplifying the process flow. With more efforts put into the colloidal stability of CNT dispersion, air stability of the resulting devices, controllability of threshold voltage tuning, and compatibility with other processing steps like polymer removal, *etc*., doping *via* direct modification of CNT-ink would be an interesting topic for future research.

4. Printable contacts for CNT-TFTs

Among a number of conductive materials identified for printed contacts of CNT-TFTs, including metallic nanostructures,[122] conductive polymers,[15] liquid metals,[123] and metallic carbon nanotubes,[122] silver nanoparticle inks stand out due to their balance between performance, stability, processability, and cost.[122,124] Being the most conductive metal in nature, electrodes printed with silver nanoparticle inks exhibit small sheet resistance, especially compared to those printed with organic or carbon-based inks. Copper offers close conductivity compared to silver with significantly lower cost, but its electrodes printed with nanoparticle inks are prone to oxidation under ambient conditions.[125] Gold or platinum nanoparticles (AuNPs or PtNPs), on the other hand, offer high stability in air, but their cost is prohibitive for most applications. In addition, AuNP and PtNP electrodes usually require high sintering temperature (250–300 °C), which is not compatible with many flexible substrates, such as PET and paper.[122,126,127] So far, a great variety of silver nanoparticle inks with different formulations have been manufactured for different printing methods discussed in section 2, including gravure printing,[16,27,28,33–35] inkjet printing,[128,129] and aerosol jet printing.[6,130] A recent study suggests that aerosol jet printing using AgNP inks produces smaller feature sizes compared to other nanostructures, such as silver nanowires (AgNWs) or nanoflakes (AgNFs) probably due to the well-established and optimized formulation of AgNP inks.[124] However, despite their common usage, well-developed formulation, and balanced properties, AgNP inks still suffer from some limitations, leaving need and opportunity for alternatives.

Although not as severe as copper, electrochemical instability poses a major challenge in the use of silver inks (Fig. 6a and b). Studies have shown that printed silver nanoparticle electrodes without any protective layer suffer from electron oxidation and migration when water is adsorbed onto the device from the moisture in air:[131]

$$2Ag + H_2O \rightarrow Ag_2O + 2H^+ + 2e^-$$

This leads to poor stability, especially for operation under humid conditions or with electrolyte gating, which will be further discussed in the next section. When compatible with the device layout, depositing a protective layer over the electrodes has been a straightforward solution. For instance, a study in 2015 reported that protective self-assembled monolayers (SAMs) of pentafluorobenzenethiol (PFBT) introduce an order of magnitude increase in the circuit duration under water-drop conditions (0.5 A between cathode and anode in a water drop).[132] However, the deposition of protective layers requires extra processing steps, which is not favorable for process flow simplicity. As a result, despite the high cost and sintering temperature, AuNP inks have been commonly used as source/drain contacts for electrolyte gated CNT-TFTs.[126,127] In addition, the conductive polymer mixture PEDOT:PSS, while exhibiting high resistivity, has been widely adopted for gate electrodes in electrolyte gating.[126,127,133,134] It's worth noting that for circuitry applications, the high cost of the AuNPs and the high resistivity of PEDOT:PSS may hinder their application in interconnects and limit their usage for contacts only.

Another challenge is that electrodes printed with nanoparticle inks usually possess limited stretchability, which is not favorable for wearable/stretchable applications. It was observed in a recent study that a 3.51% tensile strain results in partial delamination and cracking of aerosol jet-printed AgNP electrodes (Fig. 6c and d).[130] A number of intrinsically stretchable electronic materials have been demonstrated using high aspect (length to diameter) ratio silver nanowires (AgNWs), which are regarded as a promising candidate for wearable/stretchable printed electronics. Studies have shown that AgNW electrodes consisting of percolation AgNW networks are more resilient against mechanical strain compared to silver thin films (Fig. 6e).[135] The AgNWs within the networks behave like individual units capable of moving relative to each other, which helps to avoid rupture and maintain the percolation pathways under large strain. So far, a number of AgNW inks with different formulations have been developed for screen printing,[136] gravure printing,[137] inkjet printing,[46] and aerosol jet printing.[18,47,124] For instance, a screen-printable, water-based AgNW ink has been formulated with hydroxypropyl methylcellulose (HPMC), fluorosurfactant, and antifoaming agent as the additives. The printed electrodes exhibited superior stretchability, with their conductivity remaining higher than 1% of bulk silver under 70% tensile strain, as illustrated in Fig. 6e.[136] Similar to AgNWs, metallic or unsorted carbon nanotubes are also able to form percolation networks with rubbery stretchability. As shown in Fig. 6f and g, the inkjet-printed CNT-TFTs with unsorted CNT (*i.e.*, sufficient metallic nanotube content to produce conductive thin films) source, drain, and gate contacts show minimum

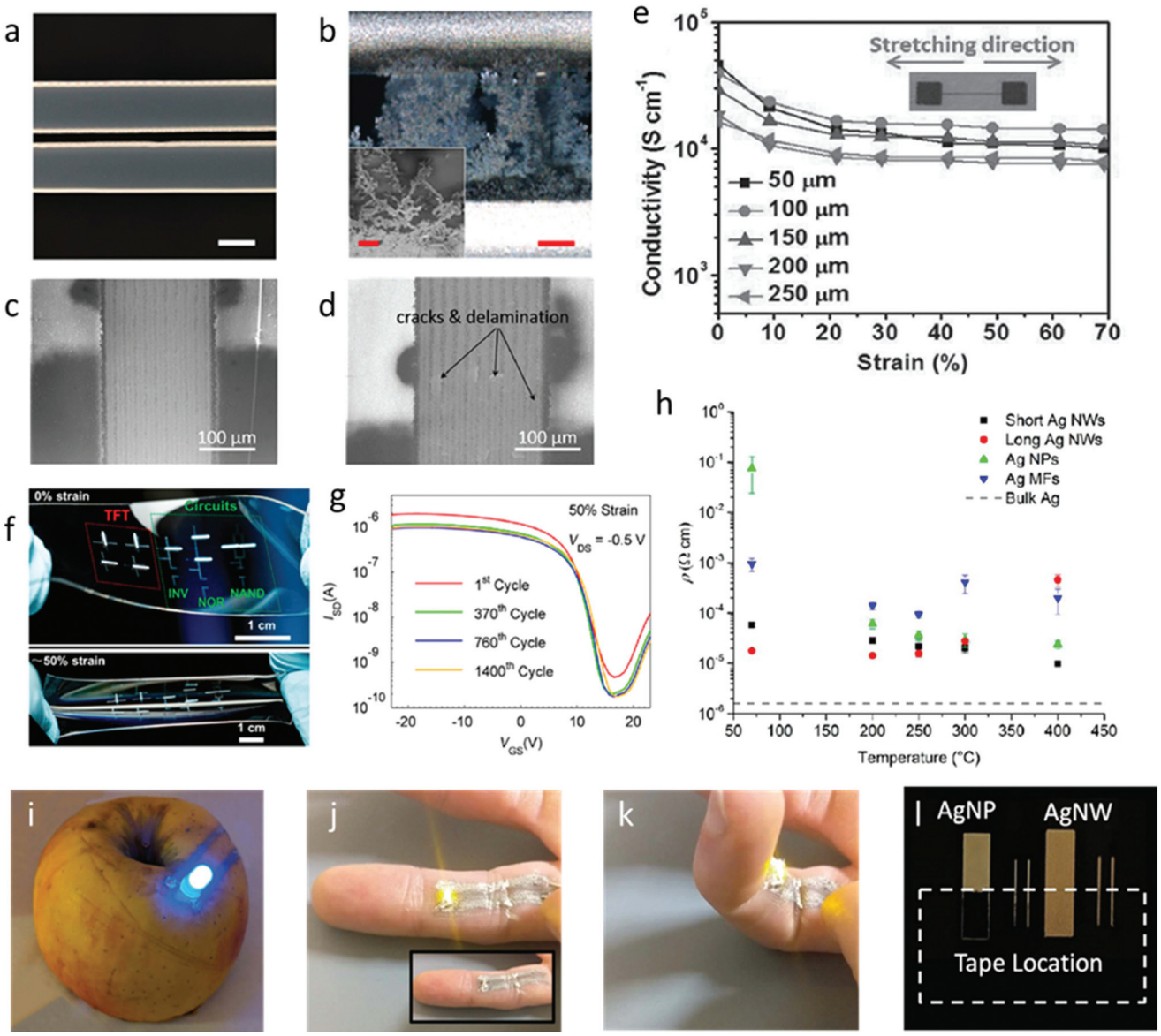

Fig. 6 Printable materials for contacts. (a) and (b) Optical images of inkjet-printed AgNP electrodes with 50 μm separation (a) before and (b) after applying 0.5 A current in water for 20 s. (c) and (d) SEM images of aerosol jet-printed AgNP electrodes after bending at (c) 1 mm and (d) 0.5 mm radius, respectively, for 1000 times. (e) Conductivity of screen-printed AgNW films with different widths plotted with respect to tensile strains. (f) Optical photographs of CNT-TFTs with unsorted CNT contacts and $BaTiO_3$/PDMS gate dielectric layer under 0% (top) and 50% (bottom) tensile strains. (g) Subthreshold characteristics of CNT-TFTs with unsorted CNT contacts while stretched for 1, 270, 760, and 1400 times. (h) Resistivity plotted as function of sintering temperature for different silver nanostructure thin films. (i)–(k) Aerosol jet-printed AgNW circuitry on (i) an apple and (j) and (k) human skin, lighting up LEDs. (l) Aerosol jet-printed AgNP and AgNW electrodes on a glass substrate after applying and removing a piece of Scotch tape. (a) and (b) Adapted with permission from ref. 132. Copyright (2018) American Chemical Society. (c) and (d) Adapted with permission from ref. 130. Copyright (2017) Wiley. (e) Adapted with permission from ref. 136. Copyright (2016) Wiley. (f) and (g) Adapted with permission from ref. 138. Copyright (2016) American Chemical Society. (h) Adapted with permission from ref. 139. Copyright (2018) American Chemical Society. (i)–(l) Adapted fromref. 47 with permission from the Royal Society of Chemistry.

drift in subthreshold performance after 1400 stretching cycles with 50% tensile strain.[138]

In addition to their high stretchability, these high-aspect-ratio nanomaterials also benefit from low sintering temperature, as well as reasonably conformal coverage on rough substrates like paper and textiles. As shown in Fig. 6h, the long (27 ± 12 μm) AgNW networked thin-film sintered at 70 °C gives resistivity lower than AgNP electrodes sintered at 200 °C.[139] More recently, N. X. Williams *et al.* reported an aqueous aerosol jet printable AgNW ink with HPMC as the binder.[47] Sintered at room temperature, the AgNW electrodes became functional once printed on glass, paper, and even bio tissues like human skin (Fig. 6i and k). In addition, after a piece of Scotch tape was applied and removed, the printed AgNW elec-

trodes also presented superior structural integrity and substrate adhesion compared to aerosol jet-printed AgNP electrodes (Fig. 6l). These findings have demonstrated the potential of printed AgNWs in a great variety of applications, including wearable, stretchable, paper, and biomedical electronics.

Contact resistance (R_c), the contribution of the metal/semiconductor interface to the total resistance, is a prevalent metric for describing the effectiveness of carrier injection and for benchmarking the contact quality after normalization by multiplication with channel width (R_cW_{CH}). Generally speaking, R_c depends on the energy levels of the contact and channel materials, as well as the metal/semiconductor interfacial quality. For high-performance nanoscale transistors, R_c plays a more and more dominant role throughout the scaling process.[140] Printed CNT-TFTs usually have a channel length ranging from tens to hundreds of micrometers, but they are nonetheless impacted by transport at the contacts and thus can benefit from contact engineering. A number of studies have reported the correlation between improved contact performance and enhanced on-current, transconductance, and mobility, which implies the significance of exploring contact engineering for CNT-TFTs.[122–124,129] C. Cao *et al.* reported that metallic CNTs give smaller R_cW_{CH} compared to AuNPs and AgNPs, as illustrated in Fig. 7a and b.[122] While the small contact resistance may offer better performance, the high sheet resistance of metallic CNTs limits their usage in contacts only, indicating the necessity of additional interconnects to avoid severe series resistances. The same work also includes a comparison across various contact geometries, and the results suggest the superiority of double contact over bottom contact over top contact (Fig. 7a and b). However, a more recent study reports that the bottom contact geometry gives higher variation across different devices (Fig. 7c).[124] It was also observed that AgNF electrodes give better contact performance to CNTs compared to AgNP and AgNW (Fig. 7d and e). This superiority is attributed to the conformal contact due to a number of factors, including coverage, surface roughness, and particle size.[124] Other than the contact material itself, modification on the CNT side could also make an impact on the interfacial properties. For instance, there have been reports showing reduced AgNP/CNT contact resistance by increasing the CNT density at the source and drain regions, as illustrated in Fig. 7f and g.[129] The high density in the source and drain region enlarge the effective contact area, bringing a 59% decrease in R_cW_{CH} together with an almost 2× increase in on-current.

With these myriad advancements taken together, it's clear that major progress has been made in the development and printing of conductive inks for use as contacts in printed CNT devices. There is not a clear universal solution; rather, the TFT geometry, printing process, and intended application will largely dictate which printable contact ink would be best to use.

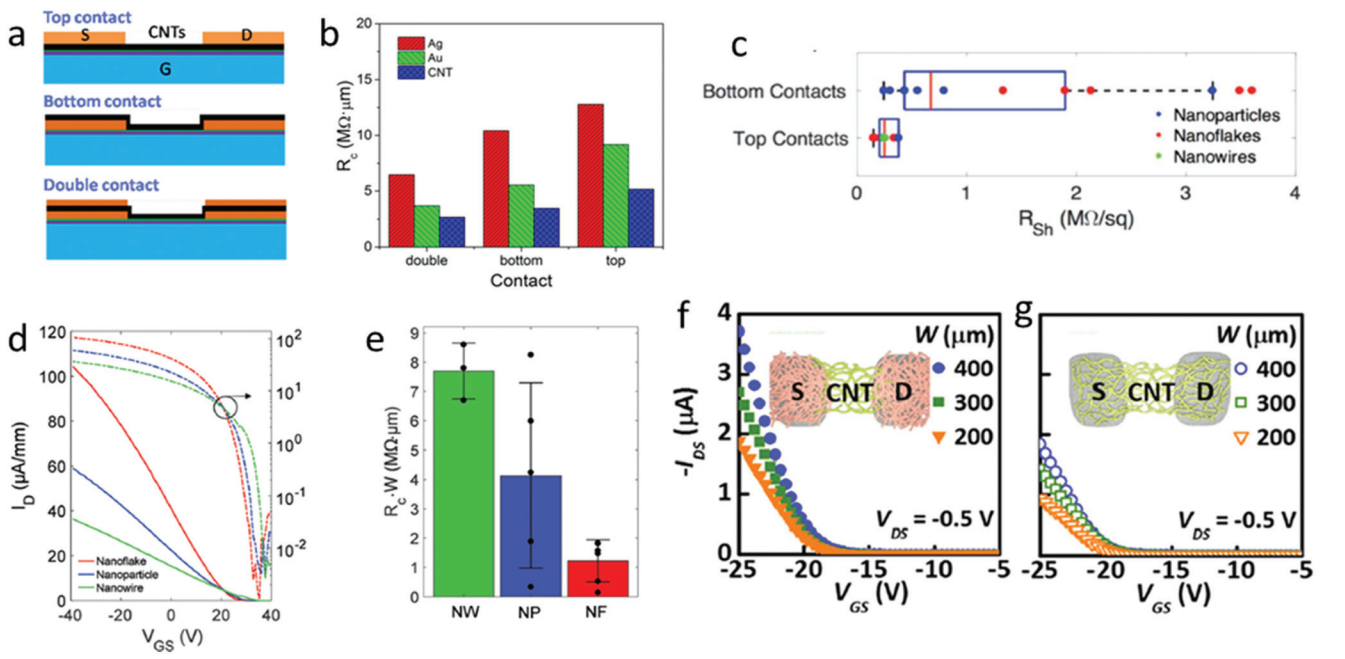

Fig. 7 Advancements in contact engineering. (a) Schematic illustrations of different contact geometries. (b) Comparison of contact resistance among CNT-TFTs with different source and drain materials and contact geometries. (c) Sheet resistance of CNT networks with different source/drain contacts. (d) Subthreshold, transfer characteristics, and (e) contact resistance of aerosol jet-printed CNT-TFTs with difference contact materials. (f) and (g) Transfer characteristics of CNT-TFTs (f) with and (g) without an increased CNT density beneath the inkjet-printed AgNP contacts. (a) and (b) Adapted with permission from ref. 122. Copyright (2016) American Chemical Society. (c)–(e) Adapted with permission from ref. 124. Copyright (2019) Wiley. (f) and (g) Adapted with permission from ref. 129. Copyright (2017) American Institute of Physics.

5. Printable dielectric materials for CNT-TFTs

The working principle of field-effect transistors, thin-film or otherwise, suggests a negative correlation between the operating voltage and gate capacitance, with a leakage-free dielectric layer having large capacitance being most favorable. For high-performance, nanoscale devices, atomic layer deposition (ALD) is a conventional technique to develop ultrathin, high-*k* gate dielectric layers with excellent uniformity, precise thickness control, and low defect density, resulting in exceptional gate control. In comparison, it is technically challenging to achieve pinhole-free dielectric films with low thickness *via* printing methods, and the thickness of printed dielectric layers are usually on the order of microns to preclude catastrophic leakage currents. Such high thickness results in rather weak gate control and high operating voltage. As a result, dielectric layers have been considered as a weak point for printed electronic devices, including CNT-TFTs, and have received considerable attention. Among a number of printable dielectric materials identified for CNT-TFTs, as summarized in Table 1, ion-gels and barium titanate ($BaTiO_3$)/polymer composite are the two most prevalent options for printed CNT-TFTs, and are each reviewed in detail below.

5.1. Ion gels and electrolyte gating

Ion gels consist of ionic liquid immobilized in polymer matrices, exhibiting ionic conductivity while remaining electrically insulating and solid-state.[141] As shown in Fig. 8a, TFTs gated through ion gels exhibit nanometer-thick electric double layers (EDLs) at the electrode/ion gel interfaces. The EDLs offer thickness-independent capacitance at the order of several μF cm^{-2}, thus facilitating printed TFTs with micrometer-thick gate insulator layers that can nevertheless function at sub-3 V operating voltage.[15,133,141] Since the formation of EDLs is determined by the ionic movements across the solid matrix, the switching speed of ion gel-gated TFTs largely depends on the ionic conductivity of the composite, which is usually limited down to a few μS.[133] A pioneering work from the group led by C. D. Frisbie demonstrated ion gel-gated CNT-TFTs with electron-beam-evaporated, photolithography-patterned Cr/Au electrodes for source and drain, and aerosol jet-printed PEDOT:PSS as the gate.[15] These CNT-TFTs facilitated inverters with 35 μs rising time, as well as 5-stage ring-oscillators with sub-50 μs stage delay and 2 kHz output frequency. Later, the same group elevated the switching speed by an order of magnitude and realized 5-stage ring oscillators with sub-5 μs stage delay, as shown in Fig. 8b–d.[133] While not comparable to modern CMOS technology, the result is still promising for applications like display backplanes.[142]

The thickness-independent nature of ELD also allows for the gate to be located on the side of the channel instead of the top. This makes it possible to print the gate electrodes in the same processing step as the source/drain electrodes, which enhances the process simplicity and reduces fabrication cost.[143] In addition, the side-gate configuration also gives rise to novel device structures like vertical electrolyte-gated transistors (VEGT), where the semiconducting channels are sandwiched vertically between the source and drain (top and bottom) electrodes, as illustrated in Fig. 8e.[144] Such structure exhibits effective channel length smaller than 100 nm, resulting in high on-current and small footprint compared to conventional lateral geometries (Fig. 8f).

As mentioned in the previous section, the ion conductivity and presence of ions in the ion gel may lead to degradation of silver electrodes, especially under high bias stress. It is shown in Fig. 8g and i that the device failure occurs with anodic corrosion of source electrodes after operating at $V_G = -1.15$ V and $V_D = -0.1$ V for a couple of minutes.[134] While replacing the silver ink with high-cost gold nanoparticle ink is a prevalent solution, avoiding direct contact between the ion gel and the silver electrode has also been proven recently to be cost-effective. As shown in Fig. 8h and j, after eliminating the silver/ion gel contact, the aerosol jet-printed CNT-TFTs showed stable performance for 2 hours under the same bias stress.[134]

Another challenge posed by ion gels is their relatively poor mechanical strength and thermal stability, and a variety of alternatives have been under exploration to offer electrolyte gating without suffering from these weaknesses. H. Li *et al.* has demonstrated a polyfluorinated electrolyte (PFE) by curing aerosol jet-printed polyfluorinated resin (PFR) and ionic liquid composite at 200 °C.[126] The resulting PFE exhibits high thermal and mechanical stability, allowing for a 300 °C sintering process for printed gold inks. The capacitance was 0.03 μF cm^{-2} at 1 kHz, which is 2 orders of magnitude lower

Table 1 Different dielectric materials for CNT-TFTs

Printable dielectric materials	Dielectric constant ε_r	Thickness (μm)	Capacitance per unit area (nF cm^{-2})	Operating voltage (V)	Notes	Ref.
Ion gels	—	—	>1000	1–3	Limited operating frequency	15, 133 and 141
Polyfluorinated electrolyte	—	34	30 @ 1 kHz	2.5	Low operating frequency; high thermal stability	126
PVDF-HFP	12.9	—	250	1	Stretchable; slow switching	146 and 147
$BaTiO_2$–polymer composite	13–17	1.5–3	5–10	10–20	High R2R compatibility	16, 28, 34–36 and 119
PVP-pMSSQ	~4	0.3–2	2–12	6–40	Low hysteresis for bottom gate	6, 130 and 153
h-BN	1.6–11.8	1.2–3	1.1–8.7	5–40	Low curing temperature	3, 23, 30 and 155

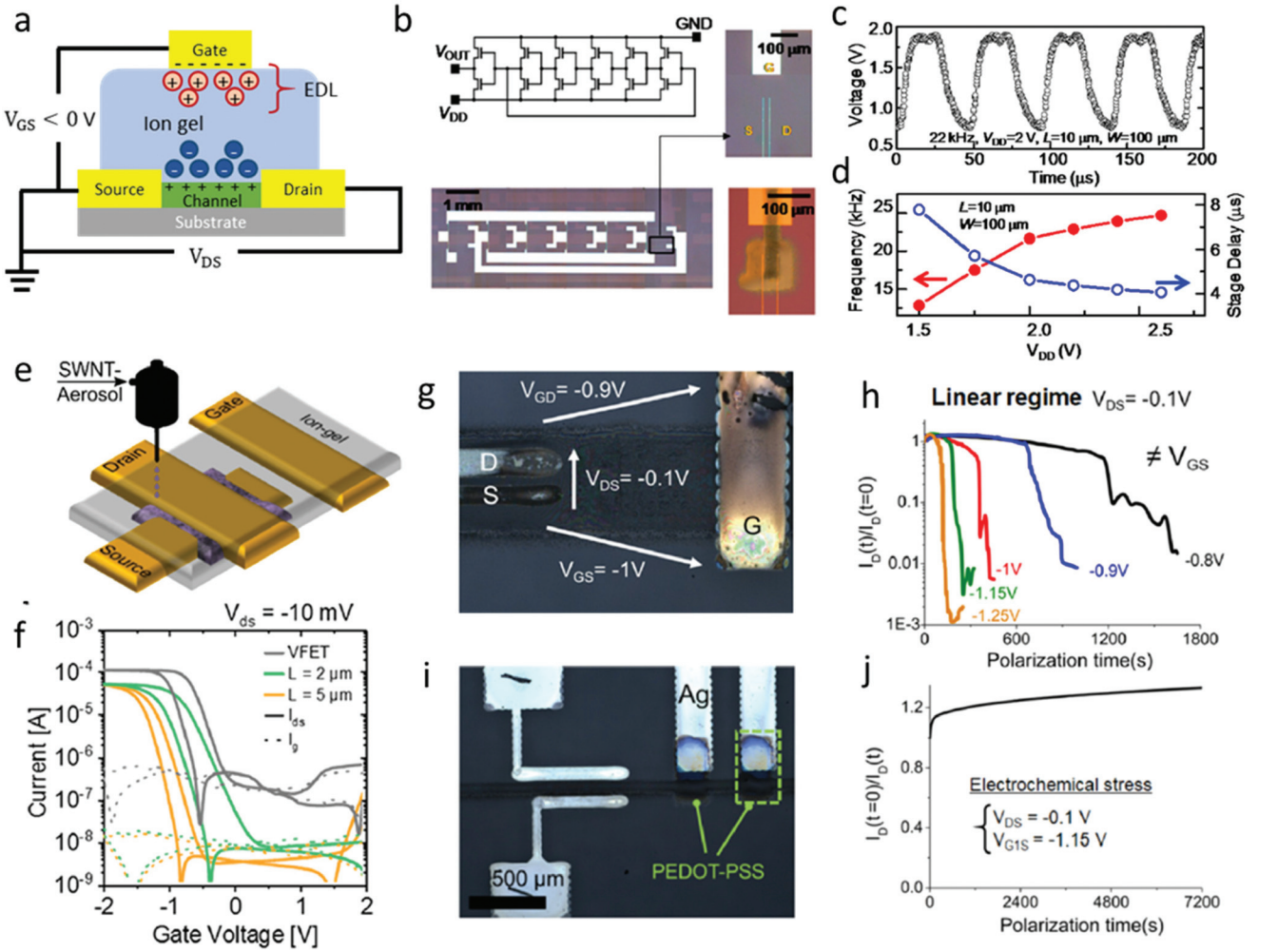

Fig. 8 Printed CNT-TFTs with ion-gel dielectrics. (a) Schematic illustration of EDLs. (b) Circuit diagram and optical images of a 5-stage ring oscillator based on aerosol jet-printed, ion gel-gated CNT-TFTs. (c) The output signal of the CNT ring oscillator showing 22 kHz frequency and 4.5 μs stage delay at V_{DD} = 2 V. (d) Frequency and stage delay of the ring oscillator plotted as functions of V_{DD}. (e) Schematic illustration of a vertical electrolyte-gated CNT transistor. (f) Comparison of transfer characteristics of between a vertical electrolyte-gated CNT transistor (CNT film thickness t = 51 nm, effective area A = 0.04 mm^2) and lateral transistors with interdigitated electrodes as the source and drain (channel width W_{CH} = 10 mm). (g) and (h) Optical images of printed ion gel-gated CNT-TFTs with ion gel (g) covering the channel and the S/D and (h) partially covering the channel. (i) and (j) Continuous bias-stress stability of printed ion gel-gated CNT-TFTs with ion gel (i) covering the channel and the S/D and (j) partially covering the channel. (b)–(d) Adapted with permission from ref. 133. Copyright (2013) American Chemical Society. (e) and (f) Adapted with permission from ref. 144. Copyright (2018) American Chemical Society. (g)–(j) Adapted with permission from ref. 134. Copyright (2019) American Chemical Society.

compared to more traditional ion gels and is likely attributed to stronger ion immobilization from the PFR. Nonetheless, the capacitance became significantly larger at low frequency ~1 Hz, facilitating sub-3 V operation of PFE-gated CNT-TFTs. In addition, arrays of PFE-gated CNT-TFTs were printed with their drain connected to light emitting diodes (LEDs), realizing display backplanes with pixel density of 170 ppi and demonstrating the potential of PFE. Another example is poly(vinylidene fluoride-*co*-hexafluoropropylene) (PVDF-HFP) developed by the group led by *Z*. Bao.[145] PVDF-HPF-gated CNT-TFTs were inkjet printed on thermoplastic styrene ethylene butylene styrene (SEBS) elastomer substrates and exhibited recoverable performance under 20% tensile strain.[146] While PVDF-HFP possesses substantially lower EDL capacitance (~250 nF cm^{-2}) and ionic conductivity (~1.2 × 10^{-10} S cm^{-1}) compared to ion gels,[147] the slow motion of ions could be utilized to mimic neural interaction, thus making it promising for bioelectronics applications such as synaptic transistors.

5.2. $BaTiO_3$/polymer composites

Increasing the dielectric permittivity of the gate insulator is a practical strategy to realize higher gate capacitance without suffering from the limited formation speed of EDLs. Incorporating high-k ceramic $BaTiO_3$ nanoparticles as nanofillers in a polymer matrix could result in a composite whose dielectric constant is substantially higher than the polymer itself, while maintaining the flexibility and printability of the polymer. Thus, $BaTiO_3$/polymer composites have been fre-

quently adopted as gate insulators for CNT-TFTs, offering ε_r up to 17, gate capacitance close to 10 nF cm^{-2}, and operating voltage V_{DD} as low as 10 V.[16] A number of $BaTiO_3$/polymer inks have been used for diverse printing methods, including inkjet printing,[128] gravure printing,[16,28,34–36,119] and screen printing.[5,17] While poly(methyl methacrylate) (PMMA) has been commonly selected as a polymer matrix,[34–36,128] the adoption of other polymers could also lead to distinct device properties. For instance, the use of $BaTiO_3$/polydimethylsiloxane (PDMS) composite leads to highly stretchable CNT-TFTs with insignificant performance change after 1400 stretching cycles with 50% tensile strain (Fig. 6f and g).[138]

Another great advantage of these mixed metal–oxide/polymer insulating materials is their R2R (and R2P) compatibility, which makes them especially favorable for large-area electronics and high-throughput manufacturing. A group led by G. Cho has pioneered this field by demonstrating R2R printable 13.56 MHz radio frequency identification (RFID) tags with one of the units being a ring oscillator based on $BaTiO_3$/PMMA-gated CNT-TFTs, as shown in Fig. 9a.[2] The same group has also demonstrated a series of digital circuits including D flip-flop,[35] half-adder,[36] *etc.*, using R2R- and R2P-printed CNT-TFTs with $BaTiO_3$/polymer dielectric layers. Later, researchers have demonstrated a great many large-area applications utilizing template-based printing of CNT-TFTs with $BaTiO_3$/polymer dielectric layers. For instance, by connecting the TFTs in an active-matrix backplane to silver/electrolyte/PEDOT:PSS electrochromic pixels, X. Cao *et al.* have fabricated active-matrix electrochromic displays *via* screen printing (Fig. 9b and c).[17] Similarly, by integrating a CNT active-matrix backplane to a pressure sensitive rubber (PSR), researchers have demonstrated R2P and R2R printing of tactile sensors with up to 20 × 20 pixels (Fig. 9d–g).[27,148]

Despite the progress, further application of R2R- or R2P-printing in the field of digital circuits using metal–oxide/polymer insulators has been hindered by the variation in threshold voltage (V_T). Through Monte Carlo simulation, a study has shown that a V_T variation less than 30% results in a 76% circuit yield of a 1-bit adder with 53 CNT-TFTs, and the yield can be pushed towards 100% by lowering the V_T variation down to 10%.[28] The equation $\Delta V_T(t) = eN_{tr}(t)/C_0$ suggests that the variation in both the trapped charge density $N_{tr}(t)$ and gate capacitance C_0 could give rise to a V_T shift. Thus, a uniform dielectric layer with no trapped charge, or at least homogeneous trapped charge density, would be preferred. In addition, a small change in rheological properties of the dielectric inks, likely caused by temperature or humidity variation, may lead to a significant difference in the resultant film's thickness, morphology, and capacitance behavior.[149] While there have been advancements in ink formulation and printing processes that improve device-to-device consistency,[33] studying the change in ink rheological properties throughout the printing process would help understand the working principle of printing methods and would provide clues for generating solutions to the variability issue.

5.3. PVP-pMSSQ blend and h-BN

Other than the prevalent ionic dielectrics and polymer/high-*k* dielectrics, together with their relatively well-established processing techniques, there have been a number of other printable dielectric materials explored recently. Poly(vinylphenol)/poly(methyl silsesquioxane) (PVP-pMSSQ, also referred to as xdi-dcs) blend has been considered as a promising gate insulator for flexible, printed CNT-TFTs. It is common for CNT transistors to exhibit large hysteresis, which is especially an issue for applications such as logic circuits where a stable V_T is

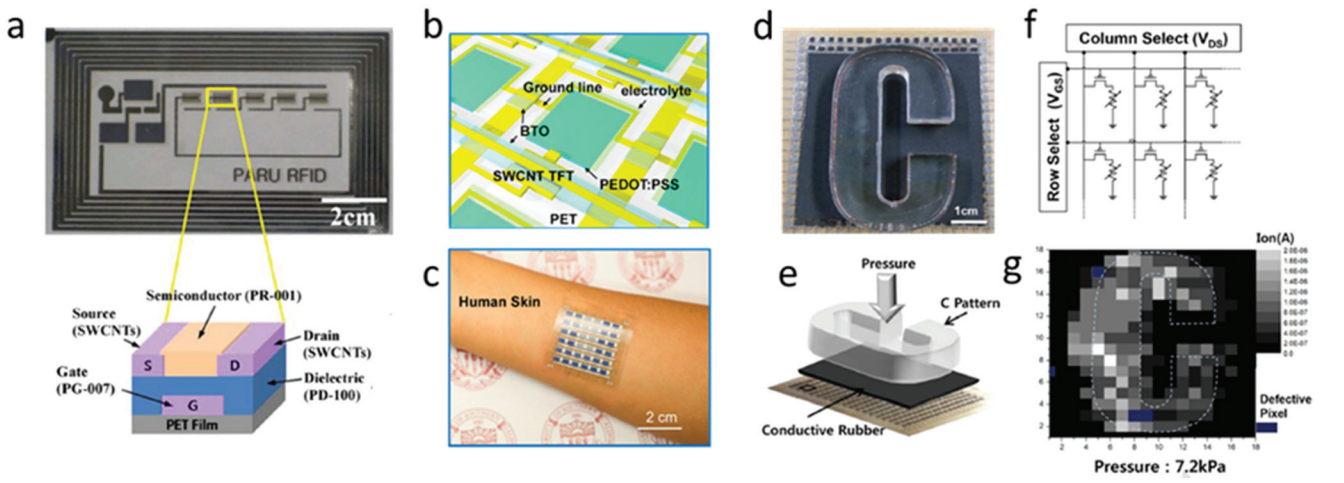

Fig. 9 Large-area electronics enabled by template-based printed, $BaTiO_3$-gated CNT-TFTs. (a) Photo of a printed RFID tag with ring oscillator based on CNT-TFTs. (b) Schematic diagram and (c) photo illustrating electrochromic displays with CNT-TFT active-matrix backplane. (d) Photo, (e) schematic diagram, and (f) circuit diagram illustrating the operation of a tactile sensor based on CNT-TFT active-matrix backplane. (g) Output currents of the backplane TFTs with 7.2 kPa pressure applied. (a) Adapted with permission from ref. 2. Copy (2010) IEEE. (b) and (c) Adapted with permission from ref. 17. Copyright (2016) American Chemical Society. (d)–(g) Adapted with permission from ref. 148. Copyright (2015) Wiley.

necessary. Charge trapping by water molecules around CNTs is a major cause of the hysteresis,[150] and a common solution is to apply an encapsulation layer atop the CNT channel.[151] However, such encapsulation steps increase process complexity and are highly undesirable for applications where the CNT channels need to be exposed. PVP-pMSSQ, on the other hand, offers strong hydrophobicity which precludes water adsorption on the dielectric/ambient interface. Thus, PVP-pMSSQ-gated CNT-TFTs exhibited stable, hysteresis-free performance in a bottom-gate configuration even without encapsulation of the CNT thin-film channel.[152] The group led by A. D. Franklin demonstrated the full aerosol jet printing of PVP-pMSSQ-gated CNT-TFTs on flexible polyimide substrates.[130] Little hysteresis was observed even in bottom-gated TFTs with CNT channels directly exposed to the ambient environment. This makes the insulator especially suitable for sensing applications, where an exposed, yet stable, CNT thin-film channel as the sensing layer is desirable. Based on the extraordinary performance, A. D. Franklin's group also developed a pressure sensor for automobile tires in more recent work.[6] As shown in Fig. 10a, the bottom-gated CNT-TFT exhibited a monotonic response to ambient pressure changes with significant sensitivity (48.1 pS PSI^{-1}).

Despite its superiority in hysteresis suppression, the printed PVP-pMSSQ layers possess a dielectric constant close to 4, with film thickness at the order of 2 μm, leading to a gate capacitance of approximately 1.8 nF cm^{-2} and an operating voltage as high as 40 V, which may cause power supply difficulties for many applications. A very recent study has achieved aerosol printing of leakage-free PVP-pMSSQ films with sub-μm thickness through careful control of ink formulation and printing parameters.[153] As illustrated in Fig. 10b and c, a thinner dielectric layer facilitates low-voltage operation, achieving sub-10 V V_{DD}.

Recently developed 2D material-based inks, produced by the large-scale liquid-phase exfoliation (LPE) methods, have also attracted considerable attention and been considered as a promising material for printed electronics.[154] Printed into nanosheet networks, the 2D insulating material hexagonal boron nitride (h-BN) can serve as a gate insulator for thin-film transistors. So far, a number of h-BN inks have been formulated for spray coating,[24,155] inkjet,[3,23] and aerosol jet printing.[30,156] While most of the reports on printed h-BN dielectric layers have used other 2D materials (*e.g.*, graphene[3,23] and MoS_2 [157]) for the channels, A. D. Franklin's group has recently developed aerosol jet printing of h-BN gated

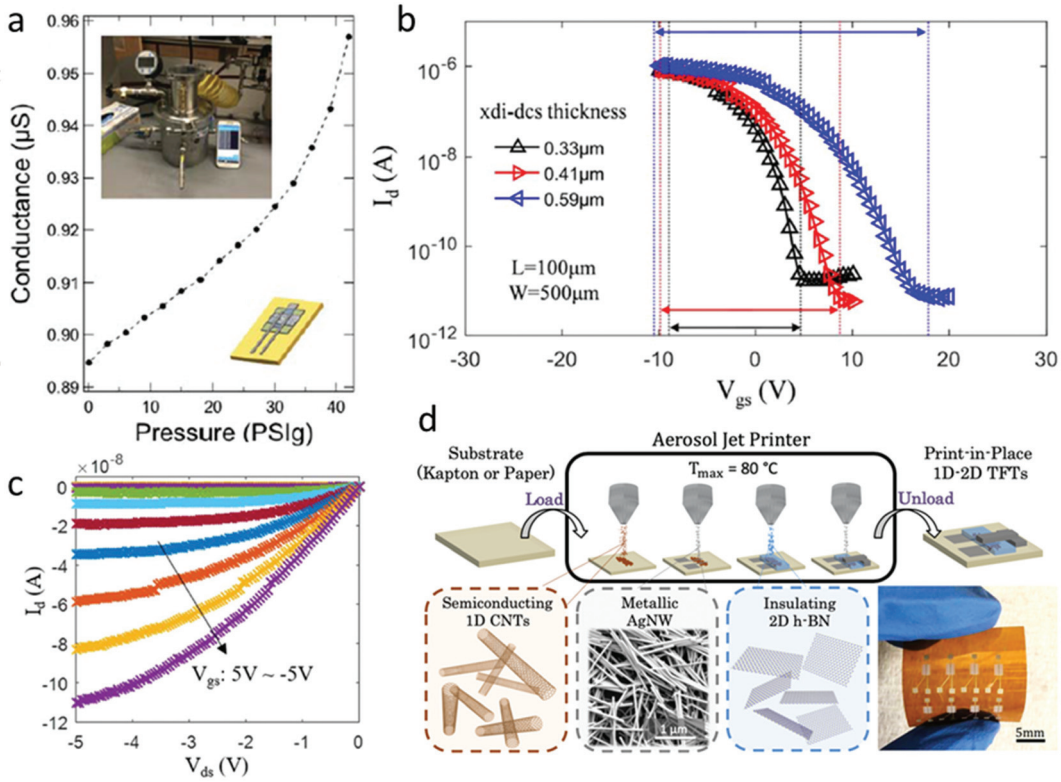

Fig. 10 Printed CNT-TFTs with PVP-pMSSQ and h-BN as gate insulators. (a) Channel conductance of a flexible CNT-TFT-based pressure sensor plotted with respect to environmental pressure. The insets include a schematic illustration of device structure as well as a photo demonstrating the experimental set up. (b) Subthreshold characteristics of PVP-pMSSQ-gated CNT-TFTs with different dielectric layer thickness. (c) Output characteristics of a PVP-pMSSQ-gated CNT-TFT with W_{CH} = 500 μm, L_{CH} = 150 μm, and a dielectric thickness of 0.3 μm. (d) In-place printing of CNT-TFTs facilitated by AgNW and h-BN inks. (a) Adapted with permission from ref. 6. Copyright (2018) IEEE. (b) and (c) Adapted with permission from ref. 153. Copyright (2020) IOP Publishing. (d) Adapted with permission from ref. 30. Copyright (2019) American Chemical Society.

CNT-TFTs with AgNW contacts, as shown in Fig. 10d. Taking advantage of the fact that none of the device layers requires any curing or sintering temperature above 80 °C, the printing process developed was fully in-place; *i.e.*, the sample stays on the printer platen throughout the entire fabrication process, free from any external curing, washing, or other processing steps away from the printer. It's worth noting that depending on the ink formulation and printing methods, the dielectric constants of printed h-BN nanosheet networks reported from different works could vary dramatically, ranging from ~1.63 to ~11.8.[3,23,30,155] Such variation calls for more detailed studies to understand the actual gating mechanism and to gain better control of the dielectric properties. In addition to dielectric gating applications, there have also been studies suggesting that porous nanosheet networks (PNNs) of h-BN can serve as matrices for electrolyte gating. Compared to the prevalent polymer matrices, h-BN PNNs have been found to offer less negative impact on ionic conductivity.[24]

6. Outlook

Despite the limited resolution and moderate mobility, which hinder the applications in RF and complex logic circuits, the combination of CNT-TFTs and printing technologies has facilitated the demonstration of large-area, flexible sensing arrays, displays, and many other devices, in a manner amenable to low-cost and large-scale fabrication. There is ample evidence of the attractive properties printed CNT thin films bring to TFTs compared to other printable semiconductors. Given the recent progress towards full print-in-place CNT-TFTs and R2R-printed CNT-TFTs, there is a versatile landscape of printing approaches available for pursuing these devices. And yet, this landscape is filled with a dizzying variety of CNT-TFT geometries and materials for printed contacts and gate dielectrics, each with their pros and cons for the electrical or mechanical (*e.g.*, flexibility) performance of the devices. While the requirements for a printed CNT-TFT technology will depend significantly on the intended application, the following ideal materials-related attributes should be pursued from the printed films:

- Uniform, high-purity semiconducting CNT thin-film channel with appropriate tube density, minimum polymer content, and controllable polarity.
- Flexible, electrochemically stable source/drain contacts with reasonable cost, low contact resistance, small sheet resistance, and processing simplicity.
- Homogeneous, high-capacitance gate dielectric allowing for fast switching and high reproducibility.

While progress has been made towards these ideal attributes, there remain significant trade-offs that must be addressed in a combined, fully printed CNT-TFT technology.

Considering the volume and variety of functional devices already developed, it is appropriate to shift part of the future efforts to benchmarking and understanding the variability and yield for printed CNT-TFTs. Rapid progress has been made in performance uniformity during the past couple of years, with sub-10% variability in threshold voltage and transconductance,[33] as well as sub-5% variability in mobility[158] reported in certain embodiments. However, due to the diversity in device configurations, performance, and applications, widely accepted criteria to benchmark performance uniformity of printed CNT-TFTs has not yet been established. Thus, the major variation factors (*e.g.*, V_T *versus* μ) for different applications, together with the most representative metrics (*e.g.*, $\sigma(V_T)/V_T$ *versus* $\sigma(V_T)/V_{DD}$) should be identified and standardized. In addition, as changes in ink rheological properties during gate insulator deposition have been considered as a major cause of V_T variation, as mentioned in section 5.2,[149] the stability of printing various inks *via* different printing methods should also be broadly and thoroughly investigated. Understanding the sources of instability and their resultant performance variability provides rationale and directions for consistency and yield enhancement.

From the materials perspective, it is also advisable to develop a set of metrics that could quantify the detailed and subtle features of printed layers. For instance, in addition to the prevalent metrics such as density and uniformity, a group led by L. Peng has proposed several metrics for quantifying and benchmarking the degree of local tube alignment of CNT films and has correlated the metrics to device performance and uniformity.[159] While the work was primarily in the field of high-performance transistors, we encourage more benchmarking metrics like these be proposed from the field of printed CNT-TFTs, examined, and appropriately adopted. Such metrics will help to understand the benefits and costs of certain techniques further, leading to a net enhancement in yield and consistency, enabling practical applications, and iteratively boosting the development of the IoE.

Conflicts of interest

Author A. D. Franklin declares a financial conflict of interest with Tyrata, Inc, which uses printed carbon nanotubes for material thickness sensing applications in tires.

References

1 Y. Zhan, Y. Mei and L. Zheng, *J. Mater. Chem. C*, 2014, **2**, 1220–1232.
2 M. Jung, J. Kim, J. Noh, N. Lim, C. Lim, G. Lee, J. Kim, H. Kang, K. Jung, A. D. Leonard, J. M. Tour and G. Cho, *IEEE Trans. Electron Devices*, 2010, **57**, 571–580.
3 R. Worsley, L. Pimpolari, D. McManus, N. Ge, R. Ionescu, J. A. Wittkopf, A. Alieva, G. Basso, M. Macucci, G. Iannaccone, K. S. Novoselov, H. Holder, G. Fiori and C. Casiraghi, *ACS Nano*, 2019, **13**, 54–60.
4 H. Shahariar, I. Kim, H. Soewardiman and J. S. Jur, *ACS Appl. Mater. Interfaces*, 2019, **11**, 6208–6216.

5 X. Cao, H. Chen, X. Gu, B. Liu, W. Wang, Y. Cao, F. Wu and C. Zhou, *ACS Nano*, 2014, **8**, 12769–12776.
6 J. B. Andrews, J. A. Cardenas, C. J. Lim, S. G. Noyce, J. Mullett and A. D. Franklin, *IEEE Sens. J.*, 2018, **18**, 7875–7880.
7 G. Grau and V. Subramanian, *Adv. Electron. Mater.*, 2016, **2**, 1500328.
8 K.-J. Baeg, D. Khim, J. Kim, D.-Y. Kim, S.-W. Sung, B.-D. Yang and Y.-Y. Noh, *IEEE Electron Device Lett.*, 2013, **34**, 126–128.
9 H. Yang, G. Zhang, J. Zhu, W. He, S. Lan, L. Liao, H. Chen and T. Guo, *J. Phys. Chem. C*, 2016, **120**, 17282–17289.
10 H. Wang, C. Cheng, L. Zhang, H. Liu, Y. Zhao, Y. Guo, W. Hu, G. Yu and Y. Liu, *Adv. Mater.*, 2014, **26**, 4683–4689.
11 K. Hong, S. H. Kim, A. Mahajan and C. D. Frisbie, *ACS Appl. Mater. Interfaces*, 2014, **6**, 18704–18711.
12 T. Kaneda, D. Hirose, T. Miyasako, P. T. Tue, Y. Murakami, S. Kohara, J. Li, T. Mitani, E. Tokumitsu and T. Shimoda, *J. Mater. Chem. C*, 2014, **2**, 40–49.
13 D. Sun, C. Chen, J. Zhang, X. Wu, H. Chen and T. Guo, *Appl. Phys. Lett.*, 2018, **112**, 012102.
14 Y. Wang, X. W. Sun, G. K. L. Goh, H. V. Demir and H. Y. Yu, *IEEE Trans. Electron Devices*, 2011, **58**, 480–485.
15 M. Ha, Y. Xia, A. A. Green, W. Zhang, M. J. Renn, C. H. Kim, C. M. Hersam and C. D. Frisbie, *ACS Nano*, 2010, **4**, 4388.
16 P. H. Lau, K. Takei, C. Wang, Y. Ju, J. Kim, Z. Yu, T. Takahashi, G. Cho and A. Javey, *Nano Lett.*, 2013, **13**, 3864–3869.
17 X. Cao, C. Lau, Y. Liu, F. Wu, H. Gui, Q. Liu, Y. Ma, H. Wan, M. R. Amer and C. Zhou, *ACS Nano*, 2016, **10**, 9816–9822.
18 J. A. Cardenas, M. J. Catenacci, J. B. Andrews, N. X. Williams, B. J. Wiley and A. D. Franklin, *ACS Appl. Nano Mater.*, 2018, **1**, 1863–1869.
19 H. Numata, K. Ihara, T. Saito, H. Endoh and F. Nihey, *Appl. Phys. Express*, 2012, **5**, 055102.
20 H. Klauk, *Chem. Soc. Rev.*, 2010, **39**, 2643–2666.
21 J. Sheng, H. J. Lee, S. Oh and J. S. Park, *ACS Appl. Mater. Interfaces*, 2016, **8**, 33821–33828.
22 F. Torrisi, T. Hasan, W. Wu, Z. Sun, A. Lombardo, T. S. Kulmala, G.-W. Hsieh, S. Jung, F. Bonaccorso, P. J. Paul, D. Chu and A. C. Ferrari, *ACS Nano*, 2012, **6**, 2992–3006.
23 T. Carey, S. Cacovich, G. Divitini, J. Ren, A. Mansouri, J. M. Kim, C. Wang, C. Ducati, R. Sordan and F. Torrisi, *Nat. Commun.*, 2017, **8**, 1202.
24 A. G. Kelly, T. Hallam, C. Backes, A. Harvey, A. S. Esmaeily, I. Godwin, J. Coelho, V. Nicolosi, J. Lauth, A. Kulkarni, S. Kinge, L. D. A. Siebbeles, G. S. Duesberg and J. N. Coleman, *Science*, 2017, **356**, 69–73.
25 T. M. Higgins, S. Finn, M. Matthiesen, S. Grieger, K. Synnatschke, M. Brohmann, M. Rother, C. Backes and J. Zaumseil, *Adv. Funct. Mater.*, 2018, **29**, 1804387.
26 M. U. Jewel, M. A. Monne, B. Mishra and M. Y. Chen, *Molecules*, 2020, **25**, 1081.
27 W. Lee, H. Koo, J. Sun, J. Noh, K. S. Kwon, C. Yeom, Y. Choi, K. Chen, A. Javey and G. Cho, *Sci. Rep.*, 2015, **5**, 17707.
28 H. Koo, W. Lee, Y. Choi, J. Sun, J. Bak, J. Noh, V. Subramanian, Y. Azuma, Y. Majima and G. Cho, *Sci. Rep.*, 2015, **5**, 14459.
29 L. Nela, J. Tang, Q. Cao, G. Tulevski and S. J. Han, *Nano Lett.*, 2018, **18**, 2054–2059.
30 S. Lu, J. A. Cardenas, R. Worsley, N. X. Williams, J. B. Andrews, C. Casiraghi and A. D. Franklin, *ACS Nano*, 2019, **13**, 11263–11272.
31 I. Jeon, J. Yoon, U. Kim, C. Lee, R. Xiang, A. Shawky, J. Xi, J. Byeon, H. M. Lee, M. Choi, S. Maruyama and Y. Matsuo, *Adv. Energy Mater.*, 2019, **9**, 1901204.
32 P. M. Grubb, F. Mokhtari Koushyar, T. Lenz, A. Asghari, G. Gan, W. Xia, H. Dalir, H. Subbaraman and R. T. Chen, *J. Manuf. Mater. Process.*, 2019, **3**, 33.
33 C. M. Homenick, R. James, G. P. Lopinski, J. Dunford, J. Sun, H. Park, Y. Jung, G. Cho and P. R. Malenfant, *ACS Appl. Mater. Interfaces*, 2016, **8**, 27900–27910.
34 J. Noh, M. Jung, K. Jung, G. Lee, S. Lim, D. Kim, S. Kim, J. M. Tour and G. Cho, *Org. Electron.*, 2011, **12**, 2185–2191.
35 J. Noh, J. Minhun, J. Kyunghwan, L. Gwangyong, K. Joonseok, L. Soyeon, K. Daae, C. Youngchul, K. Yoonjin, V. Subramanian and C. Gyoujin, *IEEE Electron Device Lett.*, 2011, **32**, 638–640.
36 J. Noh, S. Kim, K. Jung, J. Kim, S. Cho and G. Cho, *IEEE Electron Device Lett.*, 2011, **32**, 1555–1557.
37 D. Sung, A. de la Fuente Vornbrock and V. Subramanian, *IEEE Trans. Compon. Packag. Technol.*, 2010, **33**, 105–114.
38 H. Okimoto, T. Takenobu, K. Yanagi, Y. Miyata, H. Shimotani, H. Kataura and Y. Iwasa, *Adv. Mater.*, 2010, **22**, 3981–3986.
39 J. E. Fromm, *IBM J. Res. Dev.*, 1984, **28**, 322–333.
40 P. Shin, J. Sung and M. H. Lee, *Microelectron. Reliab.*, 2011, **51**, 797–804.
41 D. Jang, D. Kim and J. Moon, *Langmuir*, 2009, **25**, 2629–2635.
42 G. Hu, T. Albrow-Owen, X. Jin, A. Ali, Y. Hu, R. C. T. Howe, K. Shehzad, Z. Yang, X. Zhu, R. I. Woodward, T. C. Wu, H. Jussila, J. B. Wu, P. Peng, P. H. Tan, Z. Sun, E. J. R. Kelleher, M. Zhang, Y. Xu and T. Hasan, *Nat. Commun.*, 2017, **8**, 278.
43 R. D. Deegan, O. Bakajin, T. F. Dupont, G. Huber, S. R. Nagel and T. A. Witten, *Nature*, 1997, **389**, 827–829.
44 H. Hu and R. G. Larson, *J. Phys. Chem. B*, 2006, **110**, 7090–7094.
45 F. Torrisi, T. Hasan, W. Wu, Z. Sun, A. Lombardo, T. S. Kulmala, G.-W. Hsieh, S. Jung, F. Bonaccorso, P. J. Paul, D. Chu and A. C. Ferrari, *ACS Nano*, 2012, **6**, 2992–3006.
46 D. J. Finn, M. Lotya and J. N. Coleman, *ACS Appl. Mater. Interfaces*, 2015, **7**, 9254–9261.
47 N. X. Williams, S. Noyce, J. A. Cardenas, M. Catenacci, B. J. Wiley and A. D. Franklin, *Nanoscale*, 2019, **11**, 14294–14302.

48 *Aerosol Jet 300 Series Datasheet*, Optomec, Albuquerque, NM, U.S.A., 2016; https://www.optomec.com/wp-content/uploads/2014/04/AJ-300-Systems-Web0417.pdf.
49 A. Mahajan, C. D. Frisbie and L. F. Francis, *ACS Appl. Mater. Interfaces*, 2013, **5**, 4856–4864.
50 G. L. Goh, S. Agarwala and W. Y. Yeong, *ACS Appl. Mater. Interfaces*, 2019, **11**, 43719–43730.
51 T. Seifert, E. Sowade, F. Roscher, M. Wiemer, T. Gessner and R. R. Baumann, *Ind. Eng. Chem. Res.*, 2015, **54**, 769–779.
52 Z. Zhang, X. Liang, S. Wang, K. Yao, Y. Hu, Y. Zhu, Q. Chen, W. Zhou, Y. Li, Y. Yao, J. Zhang and L.-M. Peng, *Nano Lett.*, 2007, **7**, 3603–3607.
53 T. Durkop, S. A. Getty, E. Cobas and M. S. Fuhrer, *Nano Lett.*, 2004, **4**, 35–39.
54 P. N. Nirmalraj, P. E. Lyons, S. De, J. N. Coleman and J. J. Boland, *Nano Lett.*, 2009, **9**, 3890–3895.
55 S. Kumar, J. Y. Murthy and M. A. Alam, *Phys. Rev. Lett.*, 2005, **95**, 066802.
56 R. Saito, M. Fujita, G. Dresselhaus and M. S. Dresselhaus, *Appl. Phys. Lett.*, 1992, **60**, 2204–2206.
57 M. A. Topinka, M. W. Rowell, D. Goldhaber-Gordon, M. D. McGehee, D. S. Hecht and G. Gruner, *Nano Lett.*, 2009, **9**, 1866–1871.
58 Q. Gong, V. D. Bhatt, E. Albert, A. Abdellah, B. Fabel, P. Lugli and G. Scarpa, *IEEE Trans. Nanotechnol.*, 2014, **13**, 1181–1185.
59 S. Iijima, *Nature*, 1991, **354**, 56–58.
60 S. Iijima and T. Ichihashi, *Nature*, 1993, **363**, 603–605.
61 T. Dürkop, B. M. Kim and M. S. Fuhrer, *J. Phys.: Condens. Matter*, 2004, **16**, R553–R580.
62 J. Liu, C. Wang, X. Tu, B. Liu, L. Chen, M. Zheng and C. Zhou, *Nat. Commun.*, 2012, **3**, 1199.
63 J. Wang, X. Jin, Z. Liu, G. Yu, Q. Ji, H. Wei, J. Zhang, K. Zhang, D. Li, Z. Yuan, J. Li, P. Liu, Y. Wu, Y. Wei, J. Wang, Q. Li, L. Zhang, J. Kong, S. Fan and K. Jiang, *Nat. Catal.*, 2018, **1**, 326–331.
64 M. C. LeMieux, M. Roberts, S. Barman, Y. W. Jin, J. M. Kim and Z. Bao, *Science*, 2008, **321**, 101–104.
65 M. Zheng, A. Jagota, E. D. Semke, B. A. Diner, R. S. McLean, S. R. Lustig, R. E. Richardson and N. G. Tassi, *Nat. Mater.*, 2003, **2**, 338–342.
66 M. Zheng, A. Jagota, M. S. Strano, A. P. Santos, P. Barone, S. G. Chou, B. A. Diner, M. S. Dresselhaus, R. S. Mclean, O. G. Bibiana, G. G. Samsonidze, E. D. Semke, M. Usrey and D. J. Wall, *Science*, 2003, **302**, 1545.
67 H. Liu, T. Tanaka, Y. Urabe and H. Kataura, *Nano Lett.*, 2013, **13**, 1996–2003.
68 M. S. Arnold, A. A. Green, J. F. Hulvat, S. I. Stupp and M. C. Hersam, *Nat. Nanotechnol.*, 2006, **1**, 60–65.
69 S. Ghosh, S. M. Bachilo and R. B. Weisman, *Nat. Nanotechnol.*, 2010, **5**, 443–450.
70 C. Y. Khripin, J. A. Fagan and M. Zheng, *J. Am. Chem. Soc.*, 2013, **135**, 6822–6825.
71 X. Tu, S. Manohar, A. Jagota and M. Zheng, *Nature*, 2009, **460**, 250–253.
72 S. Y. Ju, J. Doll, I. Sharma and F. Papadimitrakopoulos, *Nat. Nanotechnol.*, 2008, **3**, 356–362.
73 H. Li, B. Zhou, Y. Lin, L. Gu, W. Wang, K. A. S. Fernando, S. Kumar, L. F. Allard and Y.-P. Sun, *J. Am. Chem. Soc.*, 2004, **126**, 1014–1015.
74 F. Chen, B. Wang, Y. Chen and L.-J. Li, *Nano Lett.*, 2007, **7**, 3013–3017.
75 A. Nish, J. Y. Hwang, J. Doig and R. J. Nicholas, *Nat. Nanotechnol.*, 2007, **2**, 640–646.
76 H. Ozawa, N. Ide, T. Fujigaya, Y. Niidome and N. Nakashima, *Chem. Lett.*, 2011, **40**, 239–241.
77 W. Gomulya, G. D. Costanzo, E. J. de Carvalho, S. Z. Bisri, V. Derenskyi, M. Fritsch, N. Frohlich, S. Allard, P. Gordiichuk, A. Herrmann, S. J. Marrink, M. C. dos Santos, U. Scherf and M. A. Loi, *Adv. Mater.*, 2013, **25**, 2948–2956.
78 V. Derenskyi, W. Gomulya, J. M. Rios, M. Fritsch, N. Frohlich, S. Jung, S. Allard, S. Z. Bisri, P. Gordiichuk, A. Herrmann, U. Scherf and M. A. Loi, *Adv. Mater.*, 2014, **26**, 5969–5975.
79 H. W. Lee, Y. Yoon, S. Park, J. H. Oh, S. Hong, L. S. Liyanage, H. Wang, S. Morishita, N. Patil, Y. J. Park, J. J. Park, A. Spakowitz, G. Galli, F. Gygi, P. H. Wong, J. B. Tok, J. M. Kim and Z. Bao, *Nat. Commun.*, 2011, **2**, 541.
80 X. Yu, D. Liu, L. Kang, Y. Yang, X. Zhang, Q. Lv, S. Qiu, H. Jin, Q. Song, J. Zhang and Q. Li, *ACS Appl. Mater. Interfaces*, 2017, **9**, 15719–15726.
81 H. Ozawa, T. Fujigaya, Y. Niidome, N. Hotta, M. Fujiki and N. Nakashima, *J. Am. Chem. Soc.*, 2011, **133**, 2651–2657.
82 H. Wang, B. Hsieh, G. Jimenez-Oses, P. Liu, C. J. Tassone, Y. Diao, T. Lei, K. N. Houk and Z. Bao, *Small*, 2015, **11**, 126–133.
83 M. Rother, M. Brohmann, S. Yang, S. B. Grimm, S. P. Schießl, A. Graf and J. Zaumseil, *Adv. Electron. Mater.*, 2017, **3**, 1700080.
84 W. Talsma, A. A. Sengrian, J. M. Salazar-Rios, H. Duim, M. Abdu-Aguye, S. Jung, S. Allard, U. Scherf and M. A. Loi, *Adv. Electron. Mater.*, 2019, **5**, 1900288.
85 J. Ouyang, J. Ding, J. Lefebvre, Z. Li, C. Guo, A. J. Kell and P. R. L. Malenfant, *ACS Nano*, 2018, **12**, 1910–1919.
86 R. Parashkov, E. Becker, T. Riedl, H. H. Johannes and W. Kowalsky, *Proc. IEEE*, 2005, **93**, 1321–1329.
87 M. Rother, S. P. Schiessl, Y. Zakharko, F. Gannott and J. Zaumseil, *ACS Appl. Mater. Interfaces*, 2016, **8**, 5571–5579.
88 M. Brohmann, F. J. Berger, M. Matthiesen, S. P. Schiessl, S. Schneider and J. Zaumseil, *ACS Nano*, 2019, **13**, 7323–7332.
89 D. Kiriya, K. Chen, H. Ota, Y. Lin, P. Zhao, Z. Yu, T. J. Ha and A. Javey, *J. Am. Chem. Soc.*, 2014, **136**, 11188–11194.
90 C. Wang, J. Zhang, K. Ryu, A. Badmaev, L. G. D. Arco and C. Zhou, *Nano Lett.*, 2009, **9**, 4285–4291.
91 H. Numata, S. Asano, F. Sasaki, T. Saito, F. Nihey and H. Kataura, 2016 IEEE 16th International Conference on Nanotechnology (IEEE-NANO), Sendai, 2016, pp. 849–852.
92 A. A. Kane, A. C. Ford, A. Nissen, K. L. Krafcik and F. Léonard, *ACS Nano*, 2014, **8**, 2477–2485.

93 B. Norton-Baker, R. Ihly, I. E. Gould, A. D. Avery, Z. R. Owczarczyk, A. J. Ferguson and J. L. Blackburn, *ACS Energy Lett.*, 2016, **1**, 1212–1220.
94 A. J. Hilmer, T. P. McNicholas, S. Lin, J. Zhang, Q. H. Wang, J. D. Mendenhall, C. Song, D. A. Heller, P. W. Barone, D. Blankschtein and M. S. Strano, *Langmuir*, 2012, **28**, 1309–1321.
95 Z. Li, J. Ding, C. Guo, J. Lefebvre and P. R. L. Malenfant, *Adv. Funct. Mater.*, 2018, **28**, 1705568.
96 S. Z. Bisri, J. Gao, V. Derenskyi, W. Gomulya, I. Iezhokin, P. Gordiichuk, A. Herrmann and M. A. Loi, *Adv. Mater.*, 2012, **24**, 6147–6152.
97 N. Izard, S. Kazaoui, K. Hata, T. Okazaki, T. Saito, S. Iijima and N. Minami, *Appl. Phys. Lett.*, 2008, **92**, 243112.
98 I. Pochorovski, H. Wang, J. I. Feldblyum, X. Zhang, A. L. Antaris and Z. Bao, *J. Am. Chem. Soc.*, 2015, **137**, 4328–4331.
99 T. Lei, X. Chen, G. Pitner, H. S. Wong and Z. Bao, *J. Am. Chem. Soc.*, 2016, **138**, 802–805.
100 Y. Joo, G. J. Brady, C. Kanimozhi, J. Ko, M. J. Shea, M. T. Strand, M. S. Arnold and P. Gopalan, *ACS Appl. Mater. Interfaces*, 2017, **9**, 28859–28867.
101 Y. Joo, G. J. Brady, M. J. Shea, M. B. Oviedo, C. Kanimozhi, S. K. Schmitt, B. M. Wong, M. S. Arnold and P. Gopalan, *ACS Nano*, 2015, **9**, 10203–10213.
102 Z. Ma, J. Han, S. Yao, S. Wang and L. M. Peng, *ACS Appl. Mater. Interfaces*, 2019, **11**, 11736–11742.
103 A. M. Dowgiallo, K. S. Mistry, J. C. Johnson, O. G. Reid and J. L. Blackburn, *J. Phys. Chem. Lett.*, 2016, **7**, 1794–1799.
104 G. J. Brady, A. J. Way, N. S. Safron, H. T. Evensen, P. Gopalan and M. S. Arnold, *Sci. Adv.*, 2016, **2**, e1601240.
105 M. Brohmann, M. Rother, S. P. Schießl, E. Preis, S. Allard, U. Scherf and J. Zaumseil, *J. Phys. Chem. C*, 2018, **122**, 19886–19896.
106 P. G. Collins, K. Bradley, M. Ishigami and A. Zettl, *Science*, 2000, **287**, 1801–1804.
107 Q. Xu, J. Zhao, V. Pecunia, W. Xu, C. Zhou, J. Dou, W. Gu, J. Lin, L. Mo, Y. Zhao and Z. Cui, *ACS Appl. Mater. Interfaces*, 2017, **9**, 12750–12758.
108 V. Derycke, R. Martel, J. Appenzeller and P. Avouris, *Appl. Phys. Lett.*, 2002, **80**, 2773–2775.
109 Y. Yang, L. Ding, J. Han, Z. Zhang and L. M. Peng, *ACS Nano*, 2017, **11**, 4124–4132.
110 J. Zhang, C. Wang, Y. Fu, Y. Che and C. Zhou, *ACS Nano*, 2011, **5**, 3284–3292.
111 T. J. Ha, K. Chen, S. Chuang, K. M. Yu, D. Kiriya and A. Javey, *Nano Lett.*, 2015, **15**, 392–397.
112 M. Shim, A. Javey, N. W. S. Kam and H. Dai, *J. Am. Chem. Soc.*, 2001, **123**, 11512–11513.
113 M. L. Geier, J. J. McMorrow, W. Xu, J. Zhu, C. H. Kim, T. J. Marks and M. C. Hersam, *Nat. Nanotechnol.*, 2015, **10**, 944–948.
114 B. R. Kang, W. J. Yu, K. K. Kim, H. K. Park, S. M. Kim, Y. Park, G. Kim, H.-J. Shin, U. J. Kim, E.-H. Lee, J.-Y. Choi and Y. H. Lee, *Adv. Funct. Mater.*, 2009, **19**, 2553–2559.
115 S. Y. Lee, S. W. Lee, S. M. Kim, W. J. Yu, Y. W. Jo and Y. H. Lee, *ACS Nano*, 2011, **3**, 2369–2375.
116 S. Schneider, M. Brohmann, R. Lorenz, Y. J. Hofstetter, M. Rother, E. Sauter, M. Zharnikov, Y. Vaynzof, H. J. Himmel and J. Zaumseil, *ACS Nano*, 2018, **12**, 5895–5902.
117 H. Wang, P. Wei, Y. Li, J. Han, H. R. Lee, B. D. Naab, N. Liu, C. Wang, E. Adijanto, B. C. Tee, S. Morishita, Q. Li, Y. Gao, Y. Cui and Z. Bao, *Proc. Natl. Acad. Sci. U. S. A.*, 2014, **111**, 4776–4781.
118 M. L. Geier, K. Moudgil, S. Barlow, S. R. Marder and M. C. Hersam, *Nano Lett.*, 2016, **16**, 4329–4334.
119 D. Kim, Y. Jung, J. Sun, C. Yeom, H. Park, D. G. Jung, Y. Ju, K. Chen, A. Javey and G. Cho, *Nanoscale*, 2016, **8**, 19876–19881.
120 M. Wei, M. Robin, L. Portilla, Y. Ren, S. Shao, L. Bai, Y. Cao, V. Pecunia, Z. Cui and J. Zhao, *Carbon*, 2020, **163**, 145–153.
121 J. M. Salazar-Rios, A. A. Sengrian, W. Talsma, H. Duim, M. Abdu-Aguye, S. Jung, N. Fröhlich, S. Allard, U. Scherf and M. A. Loi, *Adv. Electron. Mater.*, 2020, **6**, 1900789.
122 C. Cao, J. B. Andrews, A. Kumar and A. D. Franklin, *ACS Nano*, 2016, **10**, 5221–5229.
123 J. B. Andrews, K. Mondal, T. V. Neumann, J. A. Cardenas, J. Wang, D. P. Parekh, Y. Lin, P. Ballentine, M. D. Dickey and A. D. Franklin, *ACS Nano*, 2018, **12**, 5482–5488.
124 J. A. Cardenas, S. Upshaw, N. X. Williams, M. J. Catenacci, B. J. Wiley and A. D. Franklin, *Adv. Funct. Mater.*, 2019, **29**, 1805727.
125 J. Cheon, J. Lee and J. Kim, *Thin Solid Films*, 2012, **520**, 2639–2643.
126 H. Li, Y. Tang, W. Guo, H. Liu, L. Zhou and N. Smolinski, *Adv. Funct. Mater.*, 2016, **26**, 6914–6920.
127 H. Li and L. Zhou, *ACS Appl. Mater. Interfaces*, 2015, **7**, 22881–22887.
128 L. Cai, S. Zhang, J. Miao, Z. Yu and C. Wang, *Adv. Funct. Mater.*, 2015, **25**, 5698–5705.
129 Y. Lee, J. Yoon, B. Choi, H. Lee, J. Park, M. Jeon, J. Han, J. Lee, Y. Kim, D. H. Kim, D. M. Kim and S.-J. Choi, *Appl. Phys. Lett.*, 2017, **111**, 173108.
130 C. Cao, J. B. Andrews and A. D. Franklin, *Adv. Electron. Mater.*, 2017, **3**, 1700057.
131 K.-S. Kim, J.-O. Bang and S.-B. Jung, *Curr. Appl. Phys.*, 2013, **13**, S190–S194.
132 T. Sekine, J. Sato, Y. Takeda, D. Kumaki and S. Tokito, *ACS Appl. Mater. Interfaces*, 2018, **10**, 16210–16215.
133 M. Ha, J. W. Seo, P. L. Prabhumirashi, W. Zhang, M. L. Geier, M. J. Renn, C. H. Kim, M. C. Hersam and C. D. Frisbie, *Nano Lett.*, 2013, **13**, 954–960.
134 M. Robin, L. Portilla, M. Wei, T. Gao, J. Zhao, S. Shao, V. Pecunia and Z. Cui, *ACS Appl. Mater. Interfaces*, 2019, **11**, 41531–41543.
135 P. Lee, J. Lee, H. Lee, J. Yeo, S. Hong, K. H. Nam, D. Lee, S. S. Lee and S. H. Ko, *Adv. Mater.*, 2012, **24**, 3326–3332.
136 J. Liang, K. Tong and Q. Pei, *Adv. Mater.*, 2016, **28**, 5986–5996.

137 Q. Huang and Y. Zhu, *Sci. Rep.*, 2018, **8**, 15167.
138 L. Cai, S. Zhang, J. Miao, Z. Yu and C. Wang, *ACS Nano*, 2016, **10**, 11459–11468.
139 I. E. Stewart, M. J. Kim and B. J. Wiley, *ACS Appl. Mater. Interfaces*, 2017, **9**, 1870–1876.
140 S. E. Thompson and S. Parthasarathy, *Mater. Today*, 2006, **9**, 20–25.
141 J. H. Cho, J. Lee, Y. Xia, B. Kim, Y. He, M. J. Renn, T. P. Lodge and C. D. Frisbie, *Nat. Mater.*, 2008, **7**, 900–906.
142 P. Chen, Y. Fu, R. Aminirad, C. Wang, J. Zhang, K. Wang, K. Galatsis and C. Zhou, *Nano Lett.*, 2011, **11**, 5301–5308.
143 J. A. Cardenas, S. Lu, N. X. Wiliiams and A. D. Franklin, 2019 Device Research Conference (DRC), Ann Arbor, MI, USA, 2019, pp. 137–138.
144 M. Rother, A. Kruse, M. Brohmann, M. Matthiesen, S. Grieger, T. M. Higgins and J. Zaumseil, *ACS Appl. Nano Mater.*, 2018, **1**, 3616–3624.
145 C. Wang, W. Y. Lee, D. Kong, R. Pfattner, G. Schweicher, R. Nakajima, C. Lu, J. Mei, T. H. Lee, H. C. Wu, J. Lopez, Y. Diao, X. Gu, S. Himmelberger, W. Niu, J. R. Matthews, M. He, A. Salleo, Y. Nishi and Z. Bao, *Sci. Rep.*, 2015, **5**, 17849.
146 F. Molina-Lopez, T. Z. Gao, U. Kraft, C. Zhu, T. Ohlund, R. Pfattner, V. R. Feig, Y. Kim, S. Wang, Y. Yun and Z. Bao, *Nat. Commun.*, 2019, **10**, 2676.
147 D. Kong, R. Pfattner, A. Chortos, C. Lu, A. C. Hinckley, C. Wang, W.-Y. Lee, J. W. Chung and Z. Bao, *Adv. Funct. Mater.*, 2016, **26**, 4680–4686.
148 C. Yeom, K. Chen, D. Kiriya, Z. Yu, G. Cho and A. Javey, *Adv. Mater.*, 2015, **27**, 1561–1566.
149 J. Noh, M. Jung, Y. Jung, C. Yeom, M. Pyo and G. Cho, *Proc. IEEE*, 2015, **103**, 554–566.
150 W. Kim, A. Javey, O. Vermesh, Q. Wang, Y. Li and H. Dai, *Nano Lett.*, 2003, **3**, 193–198.
151 T. J. Ha, D. Kiriya, K. Chen and A. Javey, *ACS Appl. Mater. Interfaces*, 2014, **6**, 8441–8446.
152 J. Lefebvre, J. Ding, Z. Li, F. Cheng, N. Du and P. R. L. Malenfant, *Appl. Phys. Lett.*, 2015, **107**, 243301.
153 J. Chen, S. Mishra, D. Vaca, N. Kumar, W. H. Yeo, S. Sitaraman and S. Kumar, *Nanotechnology*, 2020, **31**, 235301.
154 D. McManus, S. Vranic, F. Withers, V. Sanchez-Romaguera, M. Macucci, H. Yang, R. Sorrentino, K. Parvez, S. K. Son, G. Iannaccone, K. Kostarelos, G. Fiori and C. Casiraghi, *Nat. Nanotechnol.*, 2017, **12**, 343–350.
155 A. G. Kelly, D. Finn, A. Harvey, T. Hallam and J. N. Coleman, *Appl. Phys. Lett.*, 2016, **109**, 023107.
156 A. Kelly, V. Vega-Mayoral, J. B. Boland and J. N. Coleman, *2D Mater.*, 2019, **6**, 045036.
157 S. Conti, L. Pimpolari, G. Calabrese, R. Worsley, S. Majee, D. K. Polyushkin, M. Paur, S. Pace, D. H. Keum, F. Fabbri, G. Iannaccone, M. Macucci, C. Coletti, T. Mueller, C. Casiraghi and G. Fiori, *Nat. Commun.*, 2020, **11**, 3566.
158 S. Lu, J. Zheng, J. A. Cardenas, N. X. Williams, Y. C. Lin and A. D. Franklin, *ACS Appl. Mater. Interfaces*, 2020, **12**, 43083–43089.
159 J. Zhao, L. Shen, F. Liu, P. Zhao, Q. Huang, H. Han, L. Peng and X. Liang, *Nano Res.*, 2020, **13**, 1749–1755.